Influences of hydroxyl radicals (OH) on top-down estimates of the global and regional methane budgets

Yuanhong Zhao[1], Marielle Saunois[1], Philippe Bousquet[1], Xin Lin[1,a], Antoine Berchet[1], Michaela I. Hegglin[2], Josep G. Canadell[3], Robert B. Jackson[4], Edward J. Dlugokencky[5], Ray L. Langenfelds[6], Michel Ramonet[1], Doug Worthy[7], and Bo Zheng[1]

[1] Laboratoire des Sciences du Climat et de l'Environnement, LSCE-IPSL (CEA-CNRS-UVSQ), Université Paris-Saclay, 91191 Gif-sur-Yvette, France
[2] Department of Meteorology, University of Reading, Reading, RG6 6LA, UK
[3] Global Carbon Project, CSIRO Oceans and Atmosphere, Canberra, Australian Capital Territory 2601, Australia
[4] Earth System Science Department, Woods Institute for the Environment, and Precourt Institute for Energy, Stanford University, Stanford, CA 94305, USA
[5] NOAA ESRL, 325 Broadway, Boulder, CO 80305, USA
[6] Climate Science Centre, CSIRO Oceans and Atmosphere, Aspendale, Victoria 3195, Australia
[7] Environment and Climate Change Canada, Toronto, M3H 5T4, Canada

[a] now at: Climate and Space Sciences and Engineering, University of Michigan, Ann Arbor, MI 48109, USA

Abstract

The hydroxyl radical (OH), which is the dominant sink of methane (CH$_4$), plays a key role to close the global methane budget. Previous research that assessed the impact of OH changes on the CH$_4$ budget mostly relied on box modeling inversions with a very simplified atmospheric transport and no representation of the heterogeneous spatial distribution of OH radicals. Here using a variational Bayesian inversion framework and a 3D chemical transport model, LMDz, combined with 10 different OH fields derived from chemistry-climate models (CCMI experiment), we evaluate the influence of OH burden, spatial distribution, and temporal variations on the global CH$_4$ budget. The global tropospheric mean CH$_4$-reaction-weighted [OH] ([OH]$_{GM-CH4}$) ranges 10.3-16.3$\times$10^5 molec cm^{-3} across 10 OH fields during the early 2000s, resulting in inversion-based global CH$_4$ emissions between 518 and 757Tg yr^{-1}. The uncertainties in CH$_4$ inversions induced by the different OH fields are comparable to, or even larger than the uncertainty typically given by bottom-up and top-down estimates. Based on the LMDz inversions, we estimate that a 1%-increase in OH burden leads to an increase of 4Tg yr^{-1} in the estimate of global methane emissions, which is about 25% smaller than what is estimated by box-models. The uncertainties in emissions induced by OH are largest over South America, corresponding to large inter-model differences of [OH] in this region. From the early to the late 2000s, the optimized CH$_4$ emissions increased by 21.9$\pm$5.7Tg yr^{-1} (16.6-30.0Tg yr^{-1}), of which ~25% (on average) is contributed by -0.5 to +1.8% increase in OH burden. If the CCMI models represent the OH trend properly over the 2000s, our results show that a higher increasing trend of CH$_4$ emissions is needed to match the CH$_4$ observations compared to the CH$_4$ emission trend derived using constant OH. This study strengthens the importance to reach a better representation of OH burden and of OH spatial and temporal distributions to reduce the uncertainties on the global CH$_4$ budget.

1 Introduction

Methane (CH_4) plays an important role in both climate change and air quality as a major greenhouse gas and tropospheric ozone precursor (Ciais et al., 2013). CH_4 is emitted from various anthropogenic sources including agriculture, waste, fossil fuel, and biomass burning, as well as natural sources including wetlands and other freshwater systems, geological sources, termites, and wild animals. CH_4 is removed from the atmosphere mainly by reaction with hydroxyl radical (OH) (Saunois et al. 2016, 2017). Tropospheric CH_4 levels have more than doubled between the 1850s and present-day (Etheridge et al., 1998) in response to anthropogenic emissions and climate variabilities, leading to about 0.62 W m^{-2} additional radiative forcing (Etminan et al., 2016) and increases in tropospheric ozone levels of ~5 ppbv (Fiore et al., 2008). The global CH_4 atmospheric mixing ratio stabilized in the early 2000s but resumed growing at a rate of ~5ppbv yr^{-1} since 2007 (Dlugokencky, NOAA/ESRL, 2019).

Explaining the CH_4 stabilization and renewed growth requires an accurate estimation of the CH_4 budget and its evolution, as the source-sink imbalance that is responsible for the contemporary CH_4 yearly growth only accounts for 3% of the total CH_4 burden (Turner et al., 2019). To reconcile the uncertainties in the current estimation of CH_4 emissions from various sources, the Global Carbon Project integrates top-down and bottom-up studies and approaches (Kirschke et al. 2013; Saunois et al., 2016; 2017; 2019). However, gaps still remain in global and regional CH_4 emissions estimated by top-down and bottom-up approaches, as well as within each approach (Kirschke et al. 2013; Saunois et al., 2016; Bloom et al., 2017). The top-down method, which optimizes emissions by assimilating observations in an atmospheric inversion system, is expected to reduce uncertainties of bottom-up estimates. Among the remaining causes of uncertainties in the global methane budget, the representation of CH_4 sinks, mainly from OH oxidation, is one of the largest, as seen by process-based models for atmospheric chemistry (Saunois et al., 2017).

OH is the most important tropospheric oxidizing agent determining the lifetime of many pollutants and

greenhouse gases including CH_4 (Levy, 1971). A small perturbation of OH can result in significant changes in atmospheric CH_4 through catalytic chemistry (Turner et al., 2019). Tropospheric OH is mainly produced by the reaction of excited oxygen atoms ($O(^1D)$) with water vapor (primary production) and the reaction of nitrogen oxide (NO) with hydroperoxyl radicals (HO_2) and organic peroxy radicals (RO_2)

75 (secondary production). OH is rapidly removed by carbon monoxide (CO), methane (CH_4), and non-methane volatile organic compounds (NMVOCs) (Logan et al., 1981; Lelieveld et al., 2004). Tropospheric OH has a very short lifetime of a few seconds (Logan et al., 1981; Lelieveld et al., 2004), hindering direct measurements and estimates of global OH concentrations ([OH]) and limits our current understanding of the CH_4 sink.

80

Global tropospheric [OH] is approximately 1×10^6 molec cm^{-3} as calculated by atmospheric chemistry models (Naik et al., 2013; Voulgarakis et al., 2013, Zhao et al., 2019) and inversions of 1-1-1trichloroethane (methyl chloroform, MCF) (Prinn et al., 2001; Bousquet et al., 2005; Montzka et al., 2011), resulting in a chemical lifetime of ~9 years for tropospheric CH_4 (Naik et al., 2013). However,

85 accurate estimation of [OH] magnitude, distributions, and year-to-year variations needed for CH_4 emission optimizations are still evolving. For global tropospheric [OH], both MCF inversions and atmospheric chemistry model inter-comparisons give a 10%-15% uncertainty (Prinn et al., 2001; Bousquet et al., 2005; Naik et al., 2013; Zhao et al., 2019). For [OH] spatial distributions, MCF-based inversions generally infer similar mean [OH] over both hemispheres (Bousquet et al., 2005; Patra et al.,

90 2014), while atmospheric chemistry models generally give [OH] Northern hemisphere to Southern hemisphere (N/S) ratios above 1 (e.g. Naik et al., 2013; Zhao et al., 2019). For [OH] year-to-year variations, some studies have estimated magnitudes significant enough to help explain part the stagnation in atmospheric CH_4 concentrations during the early 2000s (Rigby et al., 2008; McNorton et al., 2016; Dals øren et al., 2016; Rigby et al., 2017; Turner et al., 2017), whereas others show smaller trends and

95 inter-annual variations for [OH] (Montzka et al, 2011; Naik et al., 2013; Voulgarakis et al., 2013; Zhao et

al., 2019). In a recent study, Zhao et al.(2019) simulated CH_4 with an ensemble of OH fields and showed that uncertainties in [OH] variations could explain up to 54% of model-observation discrepancies in surface CH_4 mixing ratio changes from 2000 to 2016.

100 Current top-down estimates of the global CH_4 budget usually prescribe constant [OH] over time and attribute model-observation mismatches exclusively to CH_4 emissions (Saunois et al., 2017). The role of OH on the top-down estimation of CH_4 emissions has been mostly evaluated using two box-model inversions (e.g. Rigby et al., 2017; Turner et al., 2017). Such a simplified representation of atmospheric processes, however, does not consider spatial heterogeneities in atmospheric transport, emission

105 distributions, and OH vertical and horizontal distributions (Naus et al., 2019). Following the earlier work of Zhao et al. (2019), here we use the LMDZ-SACS(Laboratoire de Météorologie Dynamique model with Zooming capability-Simplified Atmospheric Chemistry System) 3D chemical transport model forced with 10 different OH fields derived from chemistry-climate models (Patra et al., 2011; Szopa et al., 2013; Hegglin and Lamarque, 2015; Morgenstern et al., 2017; Zhao et al., 2019; Terrenoire et al., 2019) to

110 evaluate the influence of OH distribution and trends on the global CH_4 budget as estimated by a Bayesian 4D inversion system. Section 2 briefly describes the OH fields, the inversion method, and the setups of inversion experiments. Section 3 illustrates the influence of OH on the top-down estimation of CH_4 budgets and variations, specifically: i) global, regional, and sectoral CH_4 emissions (Section 3.1), ii) emission changes between the early 2000s and late 2000s (Section 3.2), and iii) year-to-year variations in

115 methane emissions (Section 3.3). Section 4 summarizes the results and discusses the impact of OH on the current CH_4 budget.

2 Method

2.1 OH fields

120 In this study, we test the 10 OH fields presented in by Zhao et al. (2019), including 7 OH fields simulated

by chemistry-transport and chemistry-climate models from Phase 1 of the Chemistry-Climate Model Initiative (CCMI) (Hegglin and Lamarque, 2015; Morgenstern et al., 2017), 2 OH fields simulated by the Interaction with Chemistry and Aerosols (INCA) model coupled to the general circulation model of the Laboratoire de Météorologie Dynamique (LMD) model (Hauglustaine et al., 2004; Szopa et al., 2013),

125   and 1 OH field from the TRANSCOM-2011 inter-comparison exercise (Patra et al., 2011)(Table 1).

The CCMI project conducted simulations with 20 state-of-the-art atmospheric chemistry-climate and chemistry-transport models to evaluate the model's projections of atmospheric composition (Hegglin and Lamarque, 2015; Morgenstern et al., 2017). In order to force atmospheric inversions during 2000-2010,

130   we use OH fields from 7 of the 20 CCMI model simulations of REF-C1 experiments (Table 1), which were driven by observed sea surface temperatures and state-of-the-art historical forcings (covering 1960-2010). For the inversions after 2010 (only with the CESM1-WACCM model, see Section 2.3), we apply inter-annual variations of OH generated from REF-C2 experiments, which were driven by sea surface conditions calculated by the online-coupled ocean and sea ice modules. Although all of the CCMI models

135   use the same anthropogenic emission inventories, the simulated OH fields show different spatial and vertical distributions, as well as year-to-year variations (Zhao et al., 2019). The inter-model differences of OH are mainly attributable to differences in natural emissions (primarily biogenic VOCs and soil and lightning NO_x emissions) and in chemical mechanisms related to NO production and loss (Zhao et al., 2019), as well as the atmospheric transport of the chemical species in the models

140

The two INCA OH fields, INCA NMHC-AER-S and INCA NMHC are simulated by two different versions of the INCA(Interaction with Chemistry and Aerosols) chemical model coupled to LMDz (Szopa et al., 2013; Terrenoire et al., 2019). The main difference between the two simulations is that INCA NMHC-AER-S includes both gas-phase and aerosol chemistry in the whole atmosphere while INCA

145   NMHC only includes gas-phase chemistry in the troposphere (Szopa et al., 2013; Terrenoire et al., 2019).

We also include the climatological OH field used in the TransCom simulations (Patra et al., 2011), which in the troposphere uses the semi-empirical, observation-based OH field computed by Spivakovsky et al. (2000).

150   Table 1 summarizes the global tropospheric mean CH_4-reaction-weighted [OH] ([OH]$_{GM-CH4}$, [OH] weighted by reaction rate of OH with CH_4 (K_{OH+CH4})×dry air mass, Lawrence et al., 2001) and dry air mass-weighted [OH] ([OH]$_{GM-M}$), as well as inter-hemispheric ratios (N/S ratios) calculated with [OH]$_{GM-CH4}$ for the 10 OH fields used in this study. The [OH]$_{GM-CH4}$ is a better indicator of the global atmospheric oxidizing efficiency for CH_4 than [OH]$_{GM-M}$, since the latter is insensitive to the CH_4+OH reaction rate

155   increased significantly with temperature (Lawrence et al., 2001). Both the mean value ($12.3\pm3.8\times10^5$ molec cm^{-3}) and absolute range(10.3-16.3×10^5 molec cm^{-3}) of [OH]$_{GM-CH4}$ calculated for the 10 OH fields are larger than those of [OH]$_{GM-M}$ ($11.4\pm2.8\times10^5$ molec cm^{-3} and 9.4-14.4×10^5 molec cm^{-3}, respectively), as some of the OH fields show distinct vertical distributions (Zhao et al., 2019). The inter-hemispheric OH ratios range from 1.0 to 1.5, larger than ones derived from MCF inversions (e.g.

160   Bousquet et al., 2005; Patra et al., 2014). A comprehensive analysis of spatial and vertical distributions of these OH fields was presented in Zhao et al. (2019).

2.2 Inverse method

We conduct an ensemble of variational inversions of CH_4 budget that rely on Bayes' theorem (Chevallier

165   et al., 2005) with the same set of atmospheric observations of CH_4 mixing ratios but different prescribed OH fields as described in Sect. 2.1. A variational data assimilation system optimizes CH_4 emissions and sinks by minimizing the cost function J, defined as:

$$J(\boldsymbol{x}) = \frac{1}{2}(\boldsymbol{x}-\boldsymbol{x^b})^T \mathbf{B}^{-1}(\boldsymbol{x}-\boldsymbol{x^b})(\boldsymbol{x}-\boldsymbol{x^b}) + \frac{1}{2}(H(\boldsymbol{x})-\boldsymbol{y})^T \mathbf{R}^{-1}(H(\boldsymbol{x})-\boldsymbol{y}) \qquad (1)$$

where $\boldsymbol{x}$ is the control vector that includes total CH_4 emissions per 10 days at the model resolution of

170   3.75 °(in longitude)×1.85 °(in latitude) and initial conditions at longitudinal and latitudinal bands of

20 °×15 °; x^b is the prior of the control vector x; y is the observation vector of observed CH_4 mixing ratios,

here at the surface; and $H(x)$ represents the sensitivity of simulated CH_4 to emissions and sinks, for

comparison with y. $\mathbf{B}$ and $\mathbf{R}$ represent the prior and observation error covariance matrix, respectively. The

cost function J is minimized iteratively by the M1QN3 algorithm (Gilbert and Lemaréchal, 1989). We do

175   not include sinks in the control vector x but prescribe the different OH fields mentioned above.

Prior knowledge (x^b) on CH_4 emissions is provided by the Global Carbon Project (GCP, Saunois et al.,

2019). The GCP emission inventory includes time-varying anthropogenic and fire emissions and

climatology of the natural emissions. Global total CH_4 emissions of the GCP inventory are 511Tg yr^{-1} in

180   2000, increased to 562Tg yr^{-1} in 2010, and 581Tg yr^{-1} in 2016 (with soil uptake excluded). The soil uptake

of CH_4 is estimated to be 38Tg yr^{-1} with seasonal variations. Averaged over 2000-2016, the anthropogenic

sources (including biofuel emissions, agriculture, and waste) and wetlands contribute 56% and 32% of

total CH_4 emissions, respectively (Fig. S1). The prior information of emissions by sector in each grid cell

is used to separate the total optimized CH_4 emissions into four broad categories: wetlands, agriculture and

185   waste, fossil fuel, and other natural sources (biomass burning, termite, geological, and ocean emissions).

The spatial distributions of the prior emissions from the four categories averaged over 2000-2016 are

shown in Fig. S1. A detailed description of the GCP emission inventory can be found in Zhao et al. (2019)

and Saunois et al. (2019). The prior error of CH_4 fluxes is set to 100% of x^b, and the error correlation is

calculated with a correlation length of 500km over land and 1000km over the oceans for CH_4 fluxes.

190

The vector of observations (y) is generated from surface measurements of the World Data Centre for

Greenhouse Gases (WDCGG, https://gaw.kishou.go.jp/) through the WMO Global Atmospheric Watch

(WMO-GAW) program. The surface measurements include both continuous time series of hourly

afternoon observations and flask data. In total, 97 sites are included here, covering different time periods,

Atmospheric
Chemistry
and Physics
Discussions

Open Access

EGU

195 including 68 sites from the Earth System Research Laboratory from the U.S. National Oceanic and
Atmospheric Administration (NOAA/ESRL, Dlugokencky et al. (1994)), 14 sites from the Laboratoire
des Sciences du Climat et de l'Environnement (LSCE), 8 sites from Environment and Climate Change
Canada (ECCC), 4 sites from the Commonwealth Scientific and Industrial Research Organisation (CSIRO,
Francey et al. (1999)), and 3 from the Japan Meteorological Agency (JMA:
200 http://www.jma.go.jp/jma/indexe.html). The location of the sites is shown in Fig. S2.

Atmospheric CH_4 sensitivities to fluxes ($H(x)$) are simulated by LMDz5B, an offline version of the LMDz
atmospheric model (Locatelli et al., 2015), which has been widely used for CH_4 studies (e.g. Bousquet et
al., 2005; Pison et al., 2009; Lin et al., 2018; Zhao et al., 2019). LMDz5B is associated with the simplified
205 chemistry module SACS (Pison et al., 2009), which calculates the CH_4 chemical sink using prescribed
4D OH and O(^{1}D) fields. Air mass fluxes simulated by the general circulation model LMDz with
temperature and wind nudged to ERA Interim re-analysis meteorology data (Dee et al, 2011) are used to
force the transport of chemical tracers in LMDz5B every 3 hours.

210 **2.3 Model experiments**

As shown in Fig. 1, we performed six groups of inversions (Inv1 to Inv6, 34 inversions in total). The
impacts of OH on the top-down estimation of CH_4 emissions are comprehensively analyzed by comparing
the inversion results within one group or between two different groups. We analyze the overall impacts
of differences in OH burden, spatial distribution, and temporal change on CH_4 emissions (colored boxes
215 on the right in Fig. 1), and separate the impacts of OH spatial distribution and temporal variations (colored
boxes on the left in Fig. 1). The results are presented and discussed in three sections as shown in different
colors in Fig. 1.

We perform four groups of 3-year CH_4 inversion experiments using 6 to 10 OH fields (Inv1 to Inv4, Fig.

220 1), and two groups of 17-year CH$_4$ inversions from 2000 to 2016 (Inv5 and Inv6, Fig. 1) using only

CESM1-WACCM OH fields. For the short-term inversions, the first and last six months are treated as

spin-up and spin-down periods and discarded from the following analyses(to avoid edge effect). Thus we

only analyze the results over 2000/07-2002/06 (i.e. the early 2000s) for Inv1 and Inv2 and over 2007/07-

2009/06 (i.e. the late 2000s) for Inv3 and Inv4. The early 2000s and the late 2000s represent the time

225 periods with stagnant and resumed growth of atmospheric CH$_4$ mixing ratios, respectively. For the long-

term inversions, we take a one-year spin-up and spin-down and analyze the 15-year results from 2001 to

2015.

The aim of Inv1, conducted for 2000-2002 with 10 OH fields, is to quantify the influence of both OH

230 burden and spatial distributions on top-down estimates of global, regional and sectoral CH$_4$ emissions

(the brown box with the solid line, Fig. 1). To separate the influence of OH spatial distributions from that

of global mean [OH], we conduct Inv2, where all the prescribed OH fields are globally scaled to the global

[OH]$_{GM\text{-}CH4}$ value of the INCA NMHC OH field in 2000 to get the same loss of CH$_4$ by OH(scaled OH

fields). By doing so, differences in inversions of Inv2 originate solely from OH spatial distributions (the

235 brown box with the dashed line, Fig. 1).

To quantify the influence of OH on temporal CH$_4$ emission changes, we also conduct Inv3 and Inv4 over

2007-2009, with 6 scaled OH fields (instead of 10 to limit computational time). While both of the

inversions are done for 2007-2009, the OH variations during 2007-2009 and 2000-2002 are used for the

240 two inversions, respectively. Therefore, while differences of Inv3－Inv2 reveal the impact of OH on

temporal CH$_4$ emission changes (E_change_all, the yellow box with solid lines of Fig. 1), Inv4－Inv2

and Inv3－Inv4 allow separating the impacts only from OH spatial distributions (E_change_fixoh) and

temporal variations (E_change_varoh) , respectively (the yellow boxes with dashed lines in Fig. 1)

Atmospheric
Chemistry
and Physics
Discussions

245 Finally, we test the impact of OH year-to-year variations and trends on CH_4 emissions over the time period

2001-2015 by running two long-term inversions (Inv5 and Inv6) with the OH fields simulated by CESM-

WACCM only (the green box with dashed lines in Fig. 1). Inv5 is forced by the OH fields with both year-

to-year variations and trends, while Inv6 is forced by the OH fields for the year 2000. For each group,

only one experiment has done for computational reasons. We chose OH fields simulated by CESM1-

250 WACCM because it shows the largest year-to-year OH variations during 2000-2010 among the CCMI

OH fields (Zhao et al., 2019). Therefore, inversions using CESM1-WACCM OH are expected to yield an

upper limit of the influence of OH variations on CH_4 emissions as seen from atmospheric chemistry

models.

255 In the following sections, to quantify uncertainties in top-down estimations of CH_4 emissions due to OH,

we calculate OH-induced CH_4 emission differences as the standard deviation of inversion results with

different OH fields.

3 Results

260 **3.1 The impacts of OH burden and spatial distributions on CH_4 emissions in 2000-2002**

3.1.1 Global total CH_4 emissions

Based on the ensemble of the 10 different OH fields listed in Table 1, global total emissions inverted by

our system in Inv1 vary from 518 to 757Tg CH_4 yr^{-1} during the early 2000s (2000/07-2002/06), nearly

covering the CH_4 emission range derived from previous bottom-up and top-down GCP syntheses

265 (Kirschke et al., 2013; Saunois et al, 2016) (Table 2 and Fig. 2). The highest CH_4 emissions exceed 700Tg

yr^{-1} are calculated using MOCAGE and SOCOL3 OH fields, for which $[OH]_{GM-CH4}$ (15.0×10^5 and 16.3

$\times 10^5$ molec cm^{-3}) are much higher than those of other OH fields (10.3-12.6×10^5 molec cm^{-3}), leading

to a larger CH_4 sink, and as a consequence also larger CH_4 emissions due to the mass balance constraint

of atmospheric inversions. The discrepancies between top-down and bottom-up estimated CH_4 emissions

270 are mainly attributable to the overestimation of natural sources (Kirschke et al., 2013) because the OH

fields used in those top-down inversions were usually constrained by MCF, and most of them used the

TransCom OH field. However, the $[OH]_{GM-M}$ constrained by MCF still have uncertainties of more than

±10% (Prinn et al., 2001; Bousquet et al., 2005). If we exclude the MOCAGE and SOCOL3 OH fields,

the multi-model estimated $[OH]_{GM-M}$ is 10.9 ±0.9×10^5 molec cm^{-3} (with uncertainty less than ±10%),

275 which leads to global total CH_4 emissions ranging from 518 to 611Tg yr^{-1} in Inv1. This range is about

twice the range given by previous top-down inversions (Kirschke et al., 2013; Saunois et al, 2016). Our

results indicate that considering different OH fields generated by different models within top-down CH_4

inversions would help decreasing discrepancies with bottom-up estimations while leading to larger

uncertainty on the CH_4 budget.

280

Plotting top-down estimated CH_4 emissions against $[OH]_{GM-CH4}$, which directly reflects the global OH

oxidizing efficiency with respect to CH_4 (Lawrence et al., 2001), reveals that the global total CH_4

emissions vary linearly with $[OH]_{GM-CH4}$ (r^2 >0.99, Fig. 2, right panel). The top-down estimation of global

total CH_4 emissions ($EMIS_{CH4}$) can be approximately calculated as:

285 $$EMIS_{CH4}=40.4\times[OH]_{GM-CH4}+66.7 \qquad\qquad (1)$$

Where $[OH]_{GM-CH4}$ is given in unit 10^5 molec cm^{-3} and $EMIS_{CH4}$ in Tg yr^{-1}. Using box-model inversions,

previous studies calculated that a 4% (0.4×10^5molec cm^{-3}) decrease in $[OH]_{GM}$ is equivalent to an

increase of 22Tg yr^{-1} CH_4 emissions (Rigby et al., 2017; Turner et al., 2017, 2019). If we apply the same

$[OH]_{GM}$ changes in Eq.1 (0.4×10^5molec cm^{-3}), the equivalent emissions change is 16Tg yr^{-1}, about 25%

290 smaller than that given by Turner et al., (2017). This difference probably results from the different

treatment of inter-hemispheric transport and stratospheric CH_4 loss in global 3D transport models

compared to the simplified box-models (Naus et al., 2019).

3.1.2 Regional CH$_4$ emissions

295   Because of the long lifetime of CH_4 relative to OH, the top-down estimates of regional CH_4 emissions can be influenced by both global total OH burden and OH spatial distributions. In Inv2 we remove the influence of the global total OH burden by scaling all the OH fields to get the same CH_4 loss as calculated by INCA NMHC in 2000. As such, Inv2 provides the uncertainty range of CH_4 emissions induced by OH spatial distribution in both horizontal and vertical directions when assuming that the global total burden

300   of OH can be precisely constrained. Thus, Inv1(the inversions using original OH fields) and Inv2 (the inversions using scaled OH fields) yield upper (uncertainties from both global OH burden and spatial distributions) and lower (uncertainties only from OH spatial distributions) limits of influences of OH on regional CH_4 emissions, respectively. Since MOCAGE and SOCOL3 OH fields show much higher $[OH]_{GM}$ than constrained by MCF observations(~10×10^5 molec cm^{-3}, e.g. Prinn et al., 2001; Bousquet

305   et al., 2005) and give much higher estimates of CH_4 emissions (>700Tg yr^{-1}) than other OH fields, we exclude inversion results with these two OH fields from the following analyses.

    In response to both global total OH burden and inter-hemispheric OH ratios (Table 1), CH_4 emissions over northern and southern hemispheres calculated by Inv1 (Table 2) vary from 368 to 424Tg yr^{-1} (401$\pm$

310   21Tg yr^{-1}) and 138 to 187Tg yr^{-1} (166$\pm$15Tg yr^{-1}), respectively, resulting in a range in inter-hemispheric CH_4 emission difference (NH$-$SH) of 206-254Tg yr^{-1} (236$\pm$14Tg yr^{-1}). When scaling all OH fields to the same loss for Inv2, the standard deviations of hemispheric CH_4 emissions are reduced to 7Tg CH_4 yr^{-1} for both hemispheres, much smaller than those derived in Inv1 (21Tg yr^{-1} and 15Tg yr^{-1} over the northern and southern hemisphere, respectively). However, the CH_4 emission inter-hemispheric difference

315   calculated by Inv2 remains at 236$\pm$14Tg yr^{-1}, similar to that calculated by Inv1, which indicates that the hemispheric CH_4 emissions differences are mainly determined by OH spatial distributions. Without the TransCom OH simulation, the inter-hemispheric CH_4 emission difference ranges between 232 and 246Tg yr^{-1}. The TransCom OH field, for which OH N/S ratio is 1.0, leads to an inter-hemispheric CH_4 emission difference of 205Tg yr^{-1}, 35Tg yr^{-1} (27Tg yr^{-1}) smaller than the mean (minimum) inter-hemispheric

Atmospheric
Chemistry
and Physics
Discussions

320   difference calculated using other OH fields (OH N/S ratio = 1.2-1.3). Previous studies show that

differences in atmospheric transport models can lead to ±28Tg yr^{-1} uncertainties in the top-down

calculation of the inter-hemispheric CH$_4$ emission difference, using a single OH field – TransCom

(Locatelli et al., 2013). Here, using a single atmospheric transport model, but different OH fields, we find

a ±14Tg yr^{-1} uncertainty, about half of the atmospheric transport model uncertainty. Combining the two

325   studies, we could expect more than 30Tg yr^{-1} uncertainty in top-down estimates of the inter-hemispheric

CH$_4$ emission difference, based on different atmospheric models and knowledge on OH.

Fig. 3 shows the optimized and prior CH$_4$ emissions calculated by Inv1 (top) and Inv2 (bottom) over

latitudinal intervals (left panels) and large emitting regions (right panels). Compared with prior emissions,

330   nearly all the optimized latitudinal and regional emissions show the same increment direction from prior

emissions, but the magnitudes of the increment largely vary. The CH$_4$ emissions calculated by Inv1

amount to i) 147 ± 14Tg yr^{-1} and are 1-47Tg yr^{-1} higher than the prior over the southern tropical regions

($30°$S-$0°$), ii) 199 ± 14Tg yr^{-1} and are 6-45Tg yr^{-1} higher than the prior over the northern tropical regions

($0°$-$30°$N), and iii) 174 ± 8Tg yr^{-1} and are 1-26Tg yr^{-1} lower than the prior over the northern mid-latitude

335   regions ($30°$N-$60°$N). The regional emission standard deviations due to OH correspond to 11%, 8%, and

4% of prior emissions over the southern tropical, northern tropical, and northern hemisphere mid-latitude

regions, respectively. This range of uncertainty is comparable to those from different inversions given by

Saunois et al. (2016). Over the large emitting regions Europe (EU), Canada (CAN), and China (CHN),

optimized emissions are lower than the prior. The Inv1 calculated emissions show the largest absolute

340   OH induced differences over northern South America (NSA, 73 ± 9Tg yr^{-1}), South Asia (SAS, 59 ± 6Tg yr^{-1}), and China (42 ± 5Tg yr^{-1}) (Fig. 3, right panels and Table 3), which account for 15-10% of the prior

emission over the corresponding regions. At the model grid-scale, the uncertainties due to OH can be

much larger than the regional mean (middle panel of Fig. 3), for example, larger than 20% of the prior

emissions over South America and central Africa, and larger than 15% of the prior over East and South

Atmospheric
Chemistry
and Physics
Discussions

345   Asia.

We now compare the inversion results using the original OH fields (Inv1) with those using scaled OH fields (Inv2) to estimate how much the optimized regional CH_4 emission differences of Inv1 are dominated by OH spatial distributions versus the global OH burden. Applying one single global scaling

350   factor per model reduces the inter-model differences of original OH fields by 33%, 67% and 33% in the southern tropics, northern tropics, and northern mid-latitudes ($30°$-$90°N$) (Table S1). This scaling results in 57%, 93%, and 22% reduction of OH induced latitudinal CH_4 emission differences, respectively (Fig. 3, left panels, comparing standard deviations of Inv1 and Inv2). At the regional scale (Fig. 3, right panel and Table 3), the OH spatial distribution-induced CH_4 emission differences (standard deviation of Inv2)

355   account for 50% of total differences over northern mid-latitude regions (China, North America) and southern tropics (South America, with largest inter-model differences of scaled OH, Fig. S3). Over northern tropical regions (Southern Asia and Southeast Asia), the OH spatial distribution induces negligible CH_4 emission differences.

360   The comparison of Inv1 and Inv2 reveals that tropical regions are less sensitive to OH spatial distribution than mid and high latitude regions in our framework. One possble explanation could be the location of monitoring sites. Over tropical regions, surface monitoring sites are mainly located in remote places, but for $30°N$-$90°N$, there are several monitoring sites located at or near the regions with high CH_4 emission rates and OH uncertainties (e.g. North America, Europe, and downwind of East Asia). Because they are

365   more constrained by monitoring sites near source regions, emissions of $30°$-$90°N$ are found to be more sensitive to the OH spatial distributions whereas emissions over tropical regions are only constrained by remote sites and are found to be more sensitive to the global OH burden.

3.1.3 Global and regional CH$_4$ emissions per source category

Fig. 4 compares optimized and prior global total CH$_4$ emissions and the difference between the prior and optimized CH$_4$ emissions for four broad source categories: wetlands, agriculture and waste (Agri-waste), fossil fuels, and other. We attribute the optimized emissions to different source sectors depend on the relative strength of individual prior sources in each grid-cell. With original OH fields, Inv1 calculates CH$_4$ emissions of 203 ± 15Tg yr^{-1} for wetlands, 209 ± 12Tg yr^{-1} for Agri-waste, 89 ± 4Tg yr^{-1} for fossil fuel, and 66 ± 3Tg yr^{-1} for other natural sources. Optimized emissions of the four sectors are 23 ± 15Tgyr^{-1}(-2-42Tg yr^{-1}), 13 ± 12Tg yr^{-1}(-3-29Tg yr^{-1}), 5 ± 4Tg yr^{-1}(-1-9Tg yr^{-1}), and 4 ± 3Tg yr^{-1}(0.1-8Tg yr^{-1}) higher than the prior emissions, respectively. Although Inv2 is conducted with scaled OH fields and all inversions calculate similar global total CH$_4$ emissions (551 ± 2Tg yr^{-1}), optimized CH$_4$ emissions still show some uncertainties due to OH (as standard deviation) (3Tg yr^{-1} for wetland emissions and 2Tg yr^{-1} for agriculture and waste, yellow boxplots in Fig. 4), in response to different OH spatial distributions.

We have further calculated CH$_4$ emissions per source category and per region estimated by Inv1 (Fig. 5), to explore the contribution of each region to the OH-induced sectoral emission uncertainties. Wetland CH$_4$ emissions mainly dominate emissions over Northern South America, Africa, South and East Asia, and Canada. Northern South America (53 ± 7Tg yr^{-1}) and Africa (30 ± 2Tg yr^{-1}) contribute most of the global total wetland OH induced emission differences and are 1-22Tg yr^{-1} and 1-8Tg yr^{-1} higher than prior emissions, respectively. In contrast to the higher wetland emissions than prior ones over tropical regions, optimized boreal wetland emissions (Canada) are 6-9Tg yr^{-1} lower than prior emissions, consistent with lower top-down estimations than the prior given by Saunois et al. (2016). Agriculture and waste emissions are most intensive over China (25 ± 3Tg yr^{-1}) and South Asia (SAS) (39 ± 3Tg yr^{-1}). The optimized inventories show lower agriculture and waste emissions over China (0.6-10Tg yr^{-1}) and Europe (1-3Tg yr^{-1}) and much higher emissions over SAS (4-13Tg yr^{-1}) compared with the prior emission inventory. The OH induced differences in fossil fuel emissions are found mainly in China and Africa, which are 0.8-5Tg

Atmospheric
Chemistry
and Physics
Discussions

395   yr^{-1} lower and 0.6-3Tg higher than prior emissions, respectively. In agreement with the previous regional

discussion, scaling the OH (Inv2) highly reduces the uncertainties attributable to different OH over the

tropical regions but not for the mid-high latitude regions. In Inv2, the largest CH_4 emission differences

due to different OH spatial distribution are found for wetland emissions in South America (60 ± 4Tg yr^{-1}), agriculture and waste emissions in South Asia (17 ± 1Tg yr^{-1}) and China (24 ± 2Tg yr^{-1}), and fossil fuel

400   emissions in China (8 ± 0.7Tg yr-1) and Russia (9 ± 0.4Tg yr^{-1}).

Previous studies have highlighted that anthropogenic emissions over China are largely overestimated by

bottom-up emissions inventories compared with top-down estimates (Kirschke et al., 2013; Tohjima et

al., 2014; Saunois et al., 2016). In our study, total anthropogenic emissions (agriculture, waste, and fossil

405   fuel) over China are 1-15Tg yr^{-1} lower than the prior bottom-up inventory as calculated by Inv1, and 7-

14Tg yr^{-1} as calculated by Inv2, with the lowest emissions calculated with the TransCom OH field (for

both Inv1 and Inv2). The TransCom OH field is the one most widely used in current top-down CH_4

emission estimations but shows much lower [OH] over China than other OH fields (Zhao et al., 2019),

which may be due to the use of the same NO_x profile over East Asia as for remote regions based on the

410   observations of 1990s when constructing the TransCom OH field (Spivakovsky et al., 2000). Thus, the

large reduction of top-down estimated anthropogenic CH_4 emissions over China as compared to the prior

emissions may be partly due to an underestimation of [OH] over China in the TransCom field.

3.2 Impact of OH on CH_4 emission changes between 2000-2002 and 2007-2009

415   As shown in Table 4, the global mean [OH] simulated by CCMI models increased by 0.7%-1.8% from

2000-2002 to 2007-2009, in response to anthropogenic emissions and climate change (Zhao et al., 2019),

whereas the INCA-NMHC model-simulated global [OH] shows a slight decrease of 0.5%. The TransCom

OH field, being constant over time, shows no change. The global scale increase mainly results from the

combination of a higher increase in the tropics compared to the northern extra-tropics and a slight decrease

17

420 in the southern extra-tropics. As a result, the changes in OH between the two periods show different patterns between regions. We have conducted inversions for 2007-2009 with scaled OH fields (Inv3) to explore how uncertainties in OH (both spatial distribution and temporal changes) can influence the top-down estimation of temporal CH_4 emission changes from the early 2000s (2000/07-2002/06) to the late 2000s (2007/07-2009/06) (E_change_all, Inv3－Inv2). We have also performed Inv4 for 2007-2009 but

425 using OH fields of 2000-2002 to separate the differences due to different time periods, with obviously different emissions (E_change_fixoh, Inv4 － Inv2) to the ones due to temporal changes in OH (E_change_varoh, Inv3－Inv4).

3.2.1 Global total emission changes between 2000-2002 and 2007-2009

430 **Total emission changes.** Changing the inversion years and OH fields increase CH_4 emissions by 21.9 ± 5.7Tg yr^{-1} (E_change_all, 16.6-30.0Tg yr^{-1}, Table 5) from the early 2000s (Inv2) to the late 2000s (Inv3). The largest CH_4 increase of 30.0Tg yr^{-1} is estimated with CESM1-WACCM OH fields (for which OH increased by 1.8% from 2000-2002 to 2007-2009), 13.4Tg yr^{-1} higher than the smallest increase of 16.6 yr^{-1} from the INCA NMHC OH field (for which OH decreased by 0.5% from 2000-2002 to 2007-

435 2009). In Saunois et al. 2017, the min-max uncertainty range of emission changes between 2002-2006 and 2008-2012 was 16Tg yr^{-1}. This means that the uncertainty attributable to different OH spatial distribution and temporal changes(13.4Tg yr^{-1}), is comparable to the min-max uncertainty resulting from using different atmospheric chemistry transport models and observations (surface and satellite), but mostly constant OH over time(16Tg yr^{-1}, Saunois et al., 2017).

440

Spatial versus temporal OH effects. Keeping OH fields from 2000-2002 (Inv4－Inv2), top-down estimated CH_4 emissions increase only by 16.9 ± 1.9Tg yr^{-1} between the early 2000s to the late 2000s (E_change_fixoh, 14.3-19.3Tg yr^{-1}, Table 5). Only changing OH from 2000-2002 to 2007-2009 (Inv3－Inv4), top-down estimated CH_4 emissions over the late 2000s change by $+5.1\pm6.4$Tg yr^{-1}

Atmospheric
Chemistry
and Physics
Discussions

Open Access

EGU

445 (E_change_varoh, -2.7-13.5Tg yr^{-1}, Table 5) due to OH temporal variations. By comparing E_change_all, E_change_fixoh, and E_change_varoh, we estimate that, on average, OH temporal variations (E_change_varoh, 5.1±6.4Tg yr^{-1}) contribute 25% of total optimized emission changes between the early and late 2000s (E_change_all, 21.9±5.7Tg yr^{-1}, Table 5). As listed in Table 5, the largest emission increase due to OH temporal variations is calculated using MRI-ESM1r1 OH fields, for which a 1.1% global

450 increase in OH can up to double the top-down estimation of CH_4 increased from the early to the late 2000s. This result indicates that a large bias likely exists in the former top-down estimation of the CH_4 emission trend calculated without considering OH changes (Saunois et al., 2017).

Comparing E_change_all, E_change_fixoh, and E_change_varoh also allows separation of uncertainties in OH spatial distribution from uncertainties in OH temporal variations. Overall, the uncertainties in OH

455 spatial distributions and OH temporal changes lead to 1.9Tg yr^{-1} (standard deviation of E_change_fixoh) and 6.4Tg yr^{-1} (standard deviation of E_change_varoh) uncertainties in optimized CH_4 emission changes from the early 2000s to late 2000s (Table 5), respectively. These results indicate that the OH spatial distribution, which is not considered in box-models, can also contribute to the uncertainties in optimized

460 CH_4 emission changes.

3.2.2 Emission changes by source types and regions

Total emission changes. We further analyze the influence of OH (both spatial distributions and temporal variations) on the top-down estimated sectoral and regional CH_4 emission changes from the early 2000s

465 to the late 2000s (E_change_all, Inv3－Inv2). As shown in Fig. 6 (top panels), the smaller increase of the optimized global CH_4 emissions from the early 2000s to the late 2000s (E_change_all, 21.9±5.7Tg yr^{-1}) compared to the prior change (39.4Tg yr^{-1}) is mainly due to decrease in wetland emissions over the southern tropics (-4.4±1.5Tg yr^{-1}, 15°S-0°) and northern mid-latitude regions (-3.4±0.4Tg yr^{-1}, 45°N-60°N) in contrast to climatology prior wetland emissions, and a lower fossil fuel emission increase over

470   30°N-45°N (3.7 ± 0.4Tg yr^{-1}) compared to prior emission increase (8.9Tg yr^{-1}). Wetlands (-3.5$\pm$2.5Tg yr^{-1}) and agriculture and waste (14.2$\pm$2.1Tg yr^{-1}) contribute most of the total OH induced uncertainty in global total emission changes(21.9 ± 5.7Tg yr^{-1}) from the early 2000s to the late 2000s (Table 6), whereas fossil fuel emissions (8.7$\pm$0.8Tg yr^{-1}) show smaller uncertainty.

475   Considering emissions over latitudinal bands (Fig. 6, top panels), the largest spread of emission changes are found over the southern tropics (15°S –tropics, -1.3 to -6.5Tg yr^{-1}), northern subtropics (15°N-30°N, 15.5 to 20.0Tg yr^{-1}), and northern extratropical regions (30°N-45°N, 7.6 to 10.7Tg yr^{-1}). The spread over the southern tropics is dominated by emission changes from wetlands (-2.3 to -6.3Tg yr^{-1}), over northern subtropics by agriculture and waste (7.3 to 10.0Tg yr^{-1}), and over northern extratropical regions by
480   agriculture and waste (3.7 to 5.1Tg yr^{-1}) and fossil fuels (3.3 to 4.3Tg yr^{-1}). At the regional scale (Fig. 7, top panels), northern South America (-1.2 to -5.2Tg yr^{-1}), South Asia (9.1 to 12.4Tg yr^{-1}), and China (-0.1 to 4.9Tg yr^{-1}) show the largest differences in emission changes from the early 2000s to the late 2000s. The multi-inversions calculated emission changes in China disagree in sign (Fig. 7; top panels), mainly due to differences in the agriculture and waste sector, which range from 1.3Tg yr^{-1} decrease to 1.5Tg yr^{-1}
485   increase from the early 2000s to the late 2000s. Previous studies have shown that large differences exist in different top-down estimated regional and sectoral emission changes mainly due to model transport errors (Saunois et al., 2017). Here, our results show that uncertainties due to OH spatio-temporal variations can also contribute to these biases in top-down inversions.

490   **Spatial versus temporal effects.** We compare regional and sectoral E_change_all (Inv3－Inv2) with E_change_fixoh (Inv4－Inv2) and E_change_varoh (Inv3－Inv4) to separate influences of OH spatial distribution and temporal variations. As shown in the bottom panels of Fig. 6 and Fig. 7, at the regional scale, OH temporal variations mainly perturb top-down estimated CH$_4$ emission changes (Fig. 6; bottom panel) over the southern tropics (0°-15°S, -3.4-5.9Tg yr^{-1}) and northern subtropics (15°N-30°N, 0-5.4Tg

495 yr^{-1}). This corresponds to the two largest spreads observed in Fig. 7 (bottom panel) associated with wetland emissions over northern South America (-2.0-3.5Tg yr^{-1}) and with agriculture and waste emissions over South Asia (-0.2-2.6Tg yr^{-1}). Among the four emission sectors, wetland emissions (mainly southern tropical wetland) show the largest increase (2.1±3.4Tg yr^{-1}) in response to OH temporal changes (Table 6), which account for 60% of total wetland emission changes between these two periods.

500

The OH spatial distribution can lead to large uncertainties in regional CH_4 emission changes. For regional and latitudinal scales, the spreads (uncertainties) of E_change_fixoh (results from OH spatial distributions) (Fig. S4 and Fig. S5) are comparable to E_change_all (top panels of Fig. 6 and Fig. 7) as mentioned above (e.g., 2.6-5.4Tg yr^{-1} decrease over northern South America, 6.1-11.1Tg yr^{-1} increase over South Asia, and 505 -0.4-4.2Tg yr^{-1} increase over China). These results show that even if the global total OH burden is well constrained (as in Inv4 and Inv2, where all OH fields are scaled to the same [OH]$_{GM-CH4,}$ and the differences in optimized CH_4 emissions changes from the early 2000s to the late 2000s are only due to different OH spatial distributions), top-down estimates of sectoral and regional temporal CH_4 emission changes remain highly uncertain .

510

3.3 Impacts of OH on year to year variations of CH_4 emissions from 2001 to 2015

To infer the influence of OH year-to-year variations on top-down optimized long-term CH_4 emission changes, we conducted two inversions, Inv5 and Inv6. Inv5 calculates optimized CH_4 emissions from 2001-2015 with the CESM1-WACCM OH field varying from one year to the next, while Inv6 uses the 515 CESM1-WACCM OH field but fixed to the year 2000. The choice of the CESM1-WACCM OH field is explained in Sect. 2.3 above. As shown in Fig. 8, the [OH]$_{GM-CH4}$ of the CESM1-WACCM OH field increases by 0.47×10^5 molec cm^{-3} (4.2%) from 2001 to 2011 and then decreases by 0.13×10^5 molec cm^{-3} (1.1%) from 2011 to 2015.

520   With OH fixed to the year 2000 (Inv6), global CH_4 emissions stall at 550 ± 2Tg yr^{-1} during 2001-2003,

decrease to 538Tg yr^{-1} in 2004, which is different from the continuous increase of CH_4 emissions given

by the bottom-up inventory (Fig. 8, top panel). After 2004, global total CH_4 emissions show a positive

trend of 3.5 ± 1.8Tg yr^{-2} (P<0.05), but smaller than the prior bottom-up inventory (4.3 ± 0.6Tg yr^{-2}

(P<0.05)). Both stalled/decreased emissions during 2001-2004 and increasing trend after 2004 are

525   consistent with previous top-down estimations (Saunois et al., 2017).

The trend of global CH_4 emission during 2004-2016 calculated by Inv5 (using varying OH) is 4.8 ± 1.8Tg

yr^{-2} (P<0.05), which is 1.3Tg yr^{-2} (36%) higher than that calculated by Inv6 (OH fixed to 2000) due to

the small increase in [OH], and also 0.5Tg yr^{-2} higher than the prior emission trend (4.3 ± 0.6Tg yr^{-2}).

530   Accounting for the OH increasing trend leads to increasing the prior trend in Inv5 instead of decreasing

it in Inv6. When calculating the differences between Inv5 and Inv6 for different latitude intervals, we find

that before 2004, differences between Inv5 and Inv6 are mainly contributed by northern middle-latitude

regions, whereas after 2004 they are dominated by tropical regions (Fig. 8, bottom).

535   We further compare CH_4 emission trends for the four previously defined emission sectors and the ten

continental regions between Inv5 and Inv6. As shown in Fig. 9, the positive global CH_4 emission trend

during 2004-2016 is mainly contributed by anthropogenic sources from agriculture and waste, and fossil

fuel-related activities, which are 1.9 ± 0.7Tg yr^{-2}, and 2.3 ± 0.4Tg yr^{-2}, respectively, as calculated by Inv6

(fixed OH). Wetland emissions show a small negative trend (-0.5 ± 0.7Tg yr^{-2}) and other natural emissions

540   do not show a significant trend (0.04 ± 0.6Tg yr^{-2}). Both sectors show large uncertainties in their trends

reflecting large year-to-year variations. When considering [OH] variations, Inv5 estimates a higher

agriculture and waste emission trend (2.4 ± 0.8Tg yr^{-2}) compared to Inv6, mainly contributed by China

(1.5 ± 0.5Tg yr^{-2} for Inv6 versus 1.7 ± 0.5Tg yr^{-2} for Inv5) and southern South America(-0.1 ± 0.1Tg yr^{-2} for

Inv6 versus 0.1 ± 0.3Tg yr^{-2} for Inv5). Accounting for temporal OH variations the negative wetland

545   emission trend reduces to near zero (0.1 ± 0.6Tg yr^{-2}), mainly due to increased emission trends over

northern South America (-0.3 ± 0.3Tg yr^{-2} for Inv6 versus 0.2 ± 0.5Tg yr^{-2} for Inv5). In contrast to

agriculture and waste, and wetland emissions, fossil fuel emissions have a similar positive trend of

2.4 ± 0.4Tg yr^{-2} in Inv5 and Inv6. This results from a higher CH$_4$ emission trend over China calculated by

Inv5 balanced by a lower CH$_4$ emission trend over North America and Russia (0.2 ± 0.2Tg yr^{-2} for Inv6

550   versus 0.1 ± 0.3Tg yr^{-2} for Inv5) since the CESM1-WACCM OH field shows aa significant negative [OH]

trend over North America (Zhao et al., 2019).

4 Conclusions and discussion

555   In this study, we have performed six groups of variational Bayesian inversions (top-down, 34 inversions

in total) using 10 different prescribed OH fields to quantify the influence of OH burden, temporal

variations, and spatial distributions on the top-down estimation of i) global total, regional, and sectoral

CH$_4$ emissions, ii) emission changes between the early 2000s and late 2000s, and iii) year-to-year

emission variations. The top-down system estimates CH$_4$ emissions by assimilating surface observations

560   with atmospheric transport of CH$_4$ calculated by the offline version LMDz5B of the LMDz atmospheric

model using different prescribed OH fields.

Based on the ensemble of 10 original OH fields ([OH]$_{GM-CH4}$:10.3-16.3×10^5 molec cm^{-3}), the global total

CH$_4$ emissions inverted by our system in Inv1 vary from 518 to 757Tg yr^{-1} during the early 2000s, nearly

565   covering the CH$_4$ emission range calculated by previous bottom-up and top-down GCP syntheses

(Kirschke et al., 2013; Saunois et al, 2016). The top-down estimated global total CH$_4$ emission varies

linearly with [OH]$_{GM-CH4}$, and we found that 1×10^5 molec cm^{-3} (10%) higher [OH]$_{GM-CH4}$ can result in

40.4Tg yr^{-1} changes in optimized CH$_4$ emissions, which is smaller than changes inferred from box-models

most probably due to inherent simplifications in the representation of atmospheric transport and chemistry

570   in these models.

At regional scale (excluding the two highest OH fields), OH-induced CH_4 emission uncertainties are largest over northern South America (12%, standard deviation/mean), South Asia (10%), and China (12%), leading to significant uncertainties in optimized emissions from the wetland and agriculture and

575   waste sectors. By performing inversions with a globally-scaled OH field, we calculated that emission uncertainties due to different OH spatial distributions account for ~50% of total uncertainties (induced by both different OH burden and different OH spatial distributions). CH_4 emission differences due to OH spatial distributions are the largest in northern South America and China but are negligible over South Asia and other northern tropical regions. Our study shows that tropical regions appear less sensitive to

580   OH spatial distribution than mid-to-high latitude regions based on CH_4 emission optimization with surface observations.

The global CH_4 emission change between 2000-2002 and 2007-2009 as estimated by top-down inversions using 6 different OH fields, is 21.9 ± 5.7Tg yr^{-1}, of which 25% (5.1 ± 6.4Tg yr^{-1}) is contributed by OH

585   temporal variations (mainly by an increase in [OH]), while 75% can be attributed to emission changes resulting from increase in observed CH_4 mixing ratios (constant OH). Among the four emission sectors, wetland emissions (mainly southern tropical wetlands) show the largest increase of 2.1 ± 3.4Tg yr^{-1} in response to OH temporal changes, which account for 60% of total wetland emission changes between these two periods. For global total emission changes, OH spatial distributions lead to lower uncertainties

590   than temporal variations (1.9Tg yr^{-1} versus 6.4Tg yr^{-1}), but on the regional scale, OH spatial distributions and temporal variations are of equal importance for quantifying CH_4 emission changes.

As the modeled OH used here mainly shows an increase in [OH] (meaning increasing CH_4 sink) during the 2000s, our inversion using year-to-year OH variations infers a 36% higher CH_4 emission trend

Atmospheric
Chemistry
and Physics
Discussions

Open Access
EGU

595   compared with an inversion driven by climatological OH over the 2001-2015 period. The different OH

fields from CCMI models consistently show increasing OH trends during 2000-2010(Zhao et al., 2019).

These variations disagree with MCF-constrained [OH], which show a decrease after 2003/2004 (Rigby

et al., 2017; Turner et al., 2017). A drop of OH between 2006-2007 (Rigby et al., 2008, Bousquet et al.,

2011) is captured by CESM1-WACCM OH fields but with (possibly) smaller changes (1%) compared to

600   (the very uncertain) $4\pm14\%$ constraint by MCF (Rigby et al., 2008). This OH drop in 2006-2007 results

in a 6Tg yr^{-1} smaller increase of CH$_4$ emissions between 2006 and 2007 compared to that derived using

constant OH. However, such [OH] drop is treated as a year-to-year variation instead of a trend, and cannot

fully explain the resumption of CH$_4$ growth from 2006-2007. Thus, during 2004-2010, at the decadal

timescale, if the CCMI models represent the OH trend properly, a higher increasing trend of CH$_4$

605   emissions is needed to match the CH$_4$ observations (compared to the CH$_4$ emission trend derived using

constant OH). After 2010, CCMI models simulated different OH trend (Zhao et al., 2019), thus the

influence on CH$_4$ emission trend is more uncertain.

Compared to previous box-model studies (e.g. Rigby et al., 2017; Turner et al. 2017), the inversions

610   performed in this study take advantage of 4D OH fields from CCMI to better quantify impacts on regional

and sectoral emission estimations. The results indicate that OH spatial distributions, which are difficult

to obtain from MCF observations, are equally important than the OH burden for constraining CH$_4$

emissions over mid- and high- latitude regions. Also, Spatio-temporal OH variations are critical to

properly infer regional and sectoral CH$_4$ emission temporal changes.

615

Top-down inversions, particularly variational Bayesian systems, are powerful tools to infer greenhouse

gas budgets, in particular, methane the target of this study. However, they suffer from some limitations

impacting the budget uncertainty. Some work has been done regarding atmospheric transport errors (e.g.,

Locatelli et al., 2013, 2015) and sensitivity to observation constraints (Locatelli et al., 2015; Houweling

620   et al., 2000), but less on the chemistry side of the budget.

Overall, our study significantly contributes to assessing the impact of OH uncertainty on the CH_4 budget.
We have shown that it is insufficient to consider a unique OH field, constant over time, in order to fully
understand and assess the global CH_4 budget and its changes over time. Indeed, further work is needed to
625   help determining OH fields to be used in future variational top-down inversion studies to properly account
for changes in both source and sinks. There are different ways to optimize current OH fields. One way is
conducting multi-species variational inversion of OH (e.g. Zheng et al., 2019) with such HFC species
(Liang et al., 2017), formaldehyde (Glenn et al., 2019), CH_4 (Zhang et al., 2018; Maasakkers et al., 2019),
or CO (Zheng et al., 2019); another way can be to build semi-empirical OH fields by combining
630   atmospheric chemistry models and observation-based meteorological data and chemical species
concentrations (e.g. NO_x, CO, VOCs. etc) as initiated in Spivakovsky et al.(2000). These OH fields should
include a mean 3D global [OH] distribution, associated with temporal variations and uncertainties. A lot
remains to be done to better constrain the chemistry side of the global methane budget, a critical step
toward its closure.

635

Data availability
The CCMI OH fields are available at the Centre for Environmental Data Analysis
(CEDA; http://data.ceda.ac.uk/badc/wcrp-ccmi/data/CCMI-1/output; Hegglin and Lamarque, 2015), the
Natural Environment Research Council's Data Repository for Atmospheric Science and Earth
640   Observation.   The   CESM1-WACCM   outputs   for   CCMI   are   available
at http://www.earthsystemgrid.org (Climate Data Gateway at NCAR, 2019). The surface observations for
CH_4 inversions are available at the World Data Centre for Greenhouse Gases (WDCGG,
https://gaw.kishou.go.jp/, 2019). Other datasets, including INCA OH fields and optimized CH_4 emissions,
can be accessed by contacting the corresponding author.

645

Author contributions
YZ, MS, and PB designed the inversion experiments, analyzed results, and wrote the manuscript. BZ

and XL helped with data preparation and inversion setup. JC and RJ discussed the results. AB developed the LMDz code for running CH4 inversions. MH provided the CCMI OH fields. DW, ED, MR, and RL provided the atmospheric in situ data. All coauthors commented on the paper.

References

Bloom, A. A., Bowman, K. W., Lee, M., Turner, A. J., Schroeder, R., Worden, J. R., Weidner, R., McDonald, K. C., and Jacob, D. J.: A global wetland methane emissions and uncertainty dataset for atmospheric chemical transport models (WetCHARTs version 1.0), Geosci. Model Dev., 10, 2141-2156, 10.5194/gmd-10-2141-2017, 2017.

Bousquet, P., Hauglustaine, D. A., Peylin, P., Carouge, C., and Ciais, P.: Two decades of OH variability as inferred by an inversion of atmospheric transport and chemistry of methyl chloroform, Atmos. Chem. Phys., 5, 2635-2656, 10.5194/acp-5-2635-2005, 2005.

Bousquet, P., Ringeval, B., Pison, I., Dlugokencky, E. J., Brunke, E. G., Carouge, C., Chevallier, F., Fortems-Cheiney, A., Frankenberg, C., Hauglustaine, D. A., Krummel, P. B., Langenfelds, R. L., Ramonet, M., Schmidt, M., Steele, L. P., Szopa, S., Yver, C., Viovy, N., and Ciais, P.: Source attribution of the changes in atmospheric methane for 2006–2008, Atmospheric Chemistry and Physics, 11, 3689-3700, 10.5194/acp-11-3689-2011, 2011.

Chevallier, F., Fisher, M., Peylin, P., Serrar, S., Bousquet, P., Bréon, F.-M., Chédin, A., and Ciais, P.: Inferring CO2 sources and sinks from satellite observations: Method and application to TOVS data, Journal of Geophysical Research: Atmospheres, 110, D24309, 10.1029/2005jd006390, 2005.

Ciais, P., Sabine, C., Bala, G., Bopp, L., Brovkin, V., al, e., and House, J. I.: Carbon and Other Biogeochemical Cycles, in: Climate Change 2013: The Physical Science Basis. Contribution of Working Group I to the Fifth Assessment Report of the Intergovernmental Panel on Climate Change Change, Cambridge University Press, Cambridge, United Kingdom and New York, NY, USA., 465–570, 2013.

Atmospheric
Chemistry
and Physics
Discussions

Open Access

EGU

Dalsøren, S. B., Myhre, C. L., Myhre, G., Gomez-Pelaez, A. J., Søvde, O. A., Isaksen, I. S. A., Weiss, R. F., and Harth, C. M.: Atmospheric methane evolution the last 40 years, Atmospheric Chemistry and Physics, 16, 3099-3126, 10.5194/acp-16-3099-2016, 2016.

Dee, D. P., Uppala, S. M., Simmons, A. J., Berrisford, P., Poli, P., Kobayashi, S., Andrae, U., Balmaseda, M. A., Balsamo, G., Bauer, P., Bechtold, P., Beljaars, A. C. M., van de Berg, L., Bidlot, J., Bormann, N., Delsol, C., Dragani, R., Fuentes, M., Geer, A. J., Haimberger, L., Healy, S. B., Hersbach, H., Hólm, E. V., Isaksen, L., Kållberg, P., Köhler, M., Matricardi, M., McNally, A. P., Monge-Sanz, B. M., Morcrette, J.-J., Park, B.-K., Peubey, C., de Rosnay, P., Tavolato, C., Thépaut, J.-N., and Vitart, F.: The ERA-Interim reanalysis: configuration and performance of the data assimilation system, Quarterly Journal of the Royal Meteorological Society, 137, 553-597, doi:10.1002/qj.828, 2011.

Dlugokencky, E., Steele, L., Lang, P., and Masarie, K.: The growth rate and distribution of atmospheric methane, Journal of Geophysical Research: Atmospheres, 99, 17021-17043, 1994.

Dlugokencky, NOAA/ESRL ,www.esrl.noaa.gov/gmd/ccgg/trends_ch4/, 2018

Emanuel, K. A.: A Scheme for Representing Cumulus Convection in Large-Scale Models, Journal of the Atmospheric Sciences, 48, 2313-2329, doi:10.1175/1520-0469(1991)048<2313:ASFRCC>2.0.CO;2, 1991.

Etheridge, D. M., Steele, L. P., Francey, R. J., and Langenfelds, R. L.: Atmospheric methane between 1000 A.D. and present: Evidence of anthropogenic emissions and climatic variability, Journal of Geophysical Research: Atmospheres, 103, 15979-15993, 10.1029/98jd00923, 1998.

Etminan, M., Myhre, G., Highwood, E. J., and Shine, K. P.: Radiative forcing of carbon dioxide, methane, and nitrous oxide: A significant revision of the methane radiative forcing, Geophysical Research Letters, 43, 12,614-612,623, doi:10.1002/2016GL071930, 2016.

Fiore, A. M., West, J. J., Horowitz, L. W., Naik, V., and Schwarzkopf, M. D.: Characterizing the tropospheric ozone response to methane emission controls and the benefits to climate and air quality, Journal of Geophysical Research: Atmospheres, 113, 10.1029/2007jd009162, 2008.

Francey, R. J., Steele, L. P., Langenfelds, R. L., and Pak, B. C.: High Precision Long-Term Monitoring of Radiatively Active and Related Trace Gases at Surface Sites and from Aircraft in the Southern Hemisphere Atmosphere, Journal of the Atmospheric Sciences, 56, 279-285, 10.1175/1520-0469(1999)056<0279:hpltmo>2.0.co;2, 1999.

Gilbert, J. C., and Lemaréchal, C.: Some numerical experiments with variable-storage quasi-Newton algorithms, Mathematical programming, 45, 407-435, 1989.

Hegglin, M. I. and Lamarque, J.-F.: The IGAC/SPARC Chemistry-Climate Model Initiative Phase-1 (CCMI-1) model data output, NCAS British Atmospheric Data Centre, [ADD ACCESS DATE], available at:http://catalogue.ceda.ac.uk/uuid/ 9cc6b94df0f4469d8066d69b5df879d5, 2015.

Houweling, S., Dentener, F., Lelieveld, J., Walter, B., and Dlugokencky, E.: The modeling of tropospheric methane: How well can point measurements be reproduced by a global model?, Journal of Geophysical Research: Atmospheres, 105, 8981-9002, 10.1029/1999jd901149, 2000.

Kirschke, S., Bousquet, P., Ciais, P., Saunois, M., Canadell, J. G., Dlugokencky, E. J., Bergamaschi, P., Bergmann, D., Blake, D. R., Bruhwiler, L., Cameron-Smith, P., Castaldi, S., Chevallier, F., Feng, L., Fraser, A., Heimann, M., Hodson, E. L., Houweling, S., Josse, B., Fraser, P. J., Krummel, P. B., Lamarque, J.-F., Langenfelds, R. L., Le Quéré, C., Naik, V., O'Doherty, S., Palmer, P. I., Pison, I., Plummer, D., Poulter, B., Prinn, R. G., Rigby, M., Ringeval, B., Santini, M., Schmidt, M., Shindell, D. T., Simpson, I. J., Spahni, R., Steele, L. P., Strode, S. A., Sudo, K., Szopa, S., van der Werf, G. R., Voulgarakis, A., van Weele, M., Weiss, R. F., Williams, J. E., and Zeng, G.: Three decades of global methane sources and sinks, Nature Geoscience, 6, 813-823, https://doi.org/10.1038/ngeo1955, 2013.

Lawrence, M. G., Jöckel, P., and von Kuhlmann, R.: What does the global mean OH concentration tell us?, Atmos. Chem. Phys., 1, 37-49, 10.5194/acp-1-37-2001, 2001.

Lelieveld, J., Dentener, F. J., Peters, W., and Krol, M. C.: On the role of hydroxyl radicals in the self-cleansing capacity of the troposphere, Atmos. Chem. Phys., 4, 2337-2344, 10.5194/acp-4-2337-2004, 2004.

Levy, H.: Normal Atmosphere: Large Radical and Formaldehyde Concentrations Predicted, Science, 173, 141-143, 10.1126/science.173.3992.141, 1971.

Lin, X., Ciais, P., Bousquet, P., Ramonet, M., Yin, Y., Balkanski, Y., Cozic, A., Delmotte, M., Evangeliou, N., Indira, N. K., Locatelli, R., Peng, S., Piao, S., Saunois, M., Swathi, P. S., Wang, R., Yver-Kwok, C., Tiwari, Y. K., and Zhou, L.: Simulating CH4 and CO2 over South and East Asia using the zoomed chemistry transport model LMDz-INCA, Atmospheric Chemistry and Physics, 18, 9475-9497, 10.5194/acp-18-9475-2018, 2018.

Liang, Q., Chipperfield, M. P., Fleming, E. L., Abraham, N. L., Braesicke, P., Burkholder, J. B., Daniel, J. S., Dhomse, S., Fraser, P. J., Hardiman, S. C., Jackman, C. H., Kinnison, D. E., Krummel, P. B., Montzka, S. A., Morgenstern, O., McCulloch, A., Mühle, J., Newman, P. A., Orkin, V. L., Pitari, G., Prinn, R. G., Rigby, M., Rozanov, E., Stenke, A., Tummon, F., Velders, G. J. M., Visioni, D., and Weiss, R. F.: Deriving Global OH Abundance and Atmospheric Lifetimes for Long-Lived Gases: A Search for CH3CCl3 Alternatives, Journal of Geophysical Research: Atmospheres, 122, 11,914-911,933, 10.1002/2017jd026926, 2017.

Lin, X., Ciais, P., Bousquet, P., Ramonet, M., Yin, Y., Balkanski, Y., Cozic, A., Delmotte, M., Evangeliou, N., Indira, N. K., Locatelli, R., Peng, S., Piao, S., Saunois, M., Swathi, P. S., Wang, R., Yver-Kwok, C., Tiwari, Y. K., and Zhou, L.: Simulating CH4 and CO2 over South and East Asia using the zoomed chemistry transport model LMDz-INCA, Atmospheric Chemistry and Physics, 18, 9475-9497, 10.5194/acp-18-9475-2018, 2018.

Locatelli, R., Bousquet, P., Chevallier, F., Fortems-Cheney, A., Szopa, S., Saunois, M., Agusti-Panareda, A., Bergmann, D., Bian, H., Cameron-Smith, P., Chipperfield, M. P., Gloor, E., Houweling, S., Kawa, S. R., Krol, M., Patra, P. K., Prinn, R. G., Rigby, M., Saito, R., and Wilson, C.: Impact of transport model errors on the global and regional methane emissions estimated by inverse modelling, Atmos. Chem. Phys., 13, 9917-9937, 10.5194/acp-13-9917-2013, 2013.

755   Locatelli, R., Bousquet, P., Hourdin, F., Saunois, M., Cozic, A., Couvreux, F., Grandpeix, J. Y., Lefebvre,
       M. P., Rio, C., Bergamaschi, P., Chambers, S. D., Karstens, U., Kazan, V., van der Laan, S., Meijer, H. A.
       J., Moncrieff, J., Ramonet, M., Scheeren, H. A., Schlosser, C., Schmidt, M., Vermeulen, A., and Williams,
       A. G.: Atmospheric transport and chemistry of trace gases in LMDz5B: evaluation and implications for
       inverse modelling, Geosci. Model Dev., 8, 129-150, 10.5194/gmd-8-129-2015, 2015.

760   Logan, J. A., Prather, M. J., Wofsy, S. C., and McElroy, M. B.: Tropospheric chemistry: A global
       perspective, Journal of Geophysical Research, 86, 7210, 10.1029/JC086iC08p07210, 1981.

       Maasakkers, J. D., Jacob, D. J., Sulprizio, M. P., Scarpelli, T. R., Nesser, H., Sheng, J. X., Zhang, Y.,
       Hersher, M., Bloom, A. A., Bowman, K. W., Worden, J. R., Janssens-Maenhout, G., and Parker, R. J.:
       Global distribution of methane emissions, emission trends, and OH concentrations and trends inferred
765   from an inversion of GOSAT satellite data for 2010–2015, Atmos. Chem. Phys., 19, 7859-7881,
       10.5194/acp-19-7859-2019, 2019.

       McNorton, J., Chipperfield, M. P., Gloor, M., Wilson, C., Feng, W., Hayman, G. D., Rigby, M., Krummel,
       P. B., amp, apos, Doherty, S., Prinn, R. G., Weiss, R. F., Young, D., Dlugokencky, E., and Montzka, S. A.:
       Role of OH variability in the stalling of the global atmospheric CH<sub>4</sub> growth rate
770   from 1999 to 2006, Atmospheric Chemistry and Physics, 16, 7943-7956, 10.5194/acp-16-7943-2016,
       2016.

       Melton, J. R., Wania, R., Hodson, E. L., Poulter, B., Ringeval, B., Spahni, R., Bohn, T., Avis, C. A.,
       Beerling, D. J., Chen, G., Eliseev, A. V., Denisov, S. N., Hopcroft, P. O., Lettenmaier, D. P., Riley, W. J.,
       Singarayer, J. S., Subin, Z. M., Tian, H., Zürcher, S., Brovkin, V., van Bodegom, P. M., Kleinen, T., Yu,
775   Z. C., and Kaplan, J. O.: Present state of global wetland extent and wetland methane modelling:
       conclusions from a model inter-comparison project (WETCHIMP), Biogeosciences, 10, 753-788,
       10.5194/bg-10-753-2013, 2013.

       Montzka, S. A., Krol, M., Dlugokencky, E., Hall, B., Jöckel, P., and Lelieveld, J.: Small Interannual
       Variability of Global Atmospheric Hydroxyl, Science, 331, 67-69, 10.1126/science.1197640, 2011.

780   Morgenstern, O., Hegglin, M. I., Rozanov, E., amp, apos, Connor, F. M., Abraham, N. L., Akiyoshi, H.,
       Archibald, A. T., Bekki, S., Butchart, N., Chipperfield, M. P., Deushi, M., Dhomse, S. S., Garcia, R. R.,
       Hardiman, S. C., Horowitz, L. W., Jöckel, P., Josse, B., Kinnison, D., Lin, M., Mancini, E., Manyin, M.
       E., Marchand, M., Marécal, V., Michou, M., Oman, L. D., Pitari, G., Plummer, D. A., Revell, L. E., Saint-
       Martin, D., Schofield, R., Stenke, A., Stone, K., Sudo, K., Tanaka, T. Y., Tilmes, S., Yamashita, Y.,
785   Yoshida, K., and Zeng, G.: Review of the global models used within phase 1 of the Chemistry–Climate
       Model Initiative (CCMI), Geoscientific Model Development, 10, 639-671, 10.5194/gmd-10-639-2017,
       2017.

       Naik, V., Voulgarakis, A., Fiore, A. M., Horowitz, L. W., Lamarque, J. F., Lin, M., Prather, M. J., Young,
       P. J., Bergmann, D., Cameron-Smith, P. J., Cionni, I., Collins, W. J., Dalsøren, S. B., Doherty, R., Eyring,
790   V., Faluvegi, G., Folberth, G. A., Josse, B., Lee, Y. H., MacKenzie, I. A., Nagashima, T., van Noije, T. P.
       C., Plummer, D. A., Righi, M., Rumbold, S. T., Skeie, R., Shindell, D. T., Stevenson, D. S., Strode, S.,

Sudo, K., Szopa, S., and Zeng, G.: Preindustrial to present-day changes in tropospheric hydroxyl radical and methane lifetime from the Atmospheric Chemistry and Climate Model Intercomparison Project (ACCMIP), Atmospheric Chemistry and Physics, 13, 5277-5298, 10.5194/acp-13-5277-2013, 2013.

795 Naus, S., Montzka, S. A., Pandey, S., Basu, S., Dlugokencky, E. J., and Krol, M.: Constraints and biases in a tropospheric two-box model of OH, Atmos. Chem. Phys., 19, 407-424, 10.5194/acp-19-407-2019, 2019.

Patra, P. K., Houweling, S., Krol, M., Bousquet, P., Belikov, D., Bergmann, D., Bian, H., Cameron-Smith, P., Chipperfield, M. P., Corbin, K., Fortems-Cheiney, A., Fraser, A., Gloor, E., Hess, P., Ito, A., Kawa, S.
800 R., Law, R. M., Loh, Z., Maksyutov, S., Meng, L., Palmer, P. I., Prinn, R. G., Rigby, M., Saito, R., and Wilson, C.: TransCom model simulations of CH4 and related species: linking transport, surface flux and chemical loss with CH4 variability in the troposphere and lower stratosphere, Atmospheric Chemistry and Physics, 11, 12813-12837, 10.5194/acp-11-12813-2011, 2011.

Patra, P. K., Krol, M. C., Montzka, S. A., Arnold, T., Atlas, E. L., Lintner, B. R., Stephens, B. B., Xiang,
805 B., Elkins, J. W., Fraser, P. J., Ghosh, A., Hintsa, E. J., Hurst, D. F., Ishijima, K., Krummel, P. B., Miller, B. R., Miyazaki, K., Moore, F. L., Muhle, J., O'Doherty, S., Prinn, R. G., Steele, L. P., Takigawa, M., Wang, H. J., Weiss, R. F., Wofsy, S. C., and Young, D.: Observational evidence for interhemispheric hydroxyl-radical parity, Nature, 513, 219-223, 10.1038/nature13721, 2014.

Pison, I., Bousquet, P., Chevallier, F., Szopa, S., and Hauglustaine, D.: Multi-species inversion of CH4,
810 CO and H2 emissions from surface measurements, Atmos. Chem. Phys., 9, 5281-5297, 10.5194/acp-9-5281-2009, 2009.

Prinn, R. G., Huang, J., Weiss, R. F., Cunnold, D. M., Fraser, P. J., Simmonds, P. G., McCulloch, A., Harth, C., Salameh, P., O'Doherty, S., Wang, R. H. J., Porter, L., and Miller, B. R.: Evidence for Substantial Variations of Atmospheric Hydroxyl Radicals in the Past Two Decades, Science, 292, 1882-1888,
815 10.1126/science.1058673, 2001.

Rigby, M., Prinn, R. G., Fraser, P. J., Simmonds, P. G., Langenfelds, R. L., Huang, J., Cunnold, D. M., Steele, L. P., Krummel, P. B., Weiss, R. F., O'Doherty, S., Salameh, P. K., Wang, H. J., Harth, C. M., Mühle, J., and Porter, L. W.: Renewed growth of atmospheric methane, Geophysical Research Letters, 35, L22805, 10.1029/2008gl036037, 2008.

820 Rigby, M., Montzka, S. A., Prinn, R. G., White, J. W. C., Young, D., O'Doherty, S., Lunt, M. F., Ganesan, A. L., Manning, A. J., Simmonds, P. G., Salameh, P. K., Harth, C. M., Muhle, J., Weiss, R. F., Fraser, P. J., Steele, L. P., Krummel, P. B., McCulloch, A., and Park, S.: Role of atmospheric oxidation in recent methane growth, Proc Natl Acad Sci U S A, 114, 5373-5377, 10.1073/pnas.1616426114, 2017.

Saunois, M., Bousquet, P., Poulter, B., Peregon, A., Ciais, P., Canadell, J. G., Dlugokencky, E. J., Etiope,
825 G., Bastviken, D., Houweling, S., Janssens-Maenhout, G., Tubiello, F. N., Castaldi, S., Jackson, R. B., Alexe, M., Arora, V. K., Beerling, D. J., Bergamaschi, P., Blake, D. R., Brailsford, G., Brovkin, V., Bruhwiler, L., Crevoisier, C., Crill, P., Covey, K., Curry, C., Frankenberg, C., Gedney, N., Höglund-Isaksson, L., Ishizawa, M., Ito, A., Joos, F., Kim, H. S., Kleinen, T., Krummel, P., Lamarque, J. F.,

830 Langenfelds, R., Locatelli, R., Machida, T., Maksyutov, S., McDonald, K. C., Marshall, J., Melton, J. R., Morino, I., Naik, V., O'Doherty, S., Parmentier, F. J. W., Patra, P. K., Peng, C., Peng, S., Peters, G. P., Pison, I., Prigent, C., Prinn, R., Ramonet, M., Riley, W. J., Saito, M., Santini, M., Schroeder, R., Simpson, I. J., Spahni, R., Steele, P., Takizawa, A., Thornton, B. F., Tian, H., Tohjima, Y., Viovy, N., Voulgarakis, A., van Weele, M., van der Werf, G. R., Weiss, R., Wiedinmyer, C., Wilton, D. J., Wiltshire, A., Worthy, D., Wunch, D., Xu, X., Yoshida, Y., Zhang, B., Zhang, Z., and Zhu, Q.: The global methane budget 2000–

835 2012, Earth Syst. Sci. Data, 8, 697-751, 10.5194/essd-8-697-2016, 2016.

Saunois, M., Bousquet, P., Poulter, B., Peregon, A., Ciais, P., Canadell, J. G., Dlugokencky, E. J., Etiope, G., Bastviken, D., Houweling, S., Janssens-Maenhout, G., Tubiello, F. N., Castaldi, S., Jackson, R. B., Alexe, M., Arora, V. K., Beerling, D. J., Bergamaschi, P., Blake, D. R., Brailsford, G., Bruhwiler, L., Crevoisier, C., Crill, P., Covey, K., Frankenberg, C., Gedney, N., Höglund-Isaksson, L., Ishizawa, M., Ito,

840 A., Joos, F., Kim, H. S., Kleinen, T., Krummel, P., Lamarque, J. F., Langenfelds, R., Locatelli, R., Machida, T., Maksyutov, S., Melton, J. R., Morino, I., Naik, V., O'Doherty, S., Parmentier, F. J. W., Patra, P. K., Peng, C., Peng, S., Peters, G. P., Pison, I., Prinn, R., Ramonet, M., Riley, W. J., Saito, M., Santini, M., Schroeder, R., Simpson, I. J., Spahni, R., Takizawa, A., Thornton, B. F., Tian, H., Tohjima, Y., Viovy, N., Voulgarakis, A., Weiss, R., Wilton, D. J., Wiltshire, A., Worthy, D., Wunch, D., Xu, X., Yoshida, Y., Zhang,

845 B., Zhang, Z., and Zhu, Q.: Variability and quasi-decadal changes in the methane budget over the period 2000–2012, Atmos. Chem. Phys., 17, 11135-11161, 10.5194/acp-17-11135-2017, 2017.

Saunois, M., Stavert, A. R., Poulter, B., Bousquet, P., Canadell, J. G., Jackson, R. B., Raymond, P. A., Dlugokencky, E. J., Houweling, S., Patra, P. K., Ciais, P., Arora, V. K., Bastviken, D., Bergamaschi, P., Blake, D. R., Brailsford, G., Bruhwiler, L., Carlson, K. M., Carrol, M., Castaldi, S., Chandra, N.,

850 Crevoisier, C., Crill, P. M., Covey, K., Curry, C. L., Etiope, G., Frankenberg, C., Gedney, N., Hegglin, M. I., Höglund-Isakson, L., Hugelius, G., Ishizawa, M., Ito, A., Janssens-Maenhout, G., Jensen, K. M., Joos, F., Kleinen, T., Krummel, P. B., Langenfelds, R. L., Laruelle, G. G., Liu, L., Machida, T., Maksyutov, S., McDonald, K. C., McNorton, J., Miller, P. A., Melton, J. R., Morino, I., Müller, J., Murgia-Flores, F., Naik, V., Niwa, Y., Noce, S., O'Doherty, S., Parker, R. J., Peng, C., Peng, S., Peters, G. P., Prigent, C.,

855 Prinn, R., Ramonet, M., Regnier, P., Riley, W. J., Rosentreter, J. A., Segers, A., Simpson, I. J., Shi, H., Smith, S. J., Steele, L. P., Thornton, B. F., Tian, H., Tohjima, Y., Tubiello, F. N., Tsuruta, A., Viovy, N., Voulgarakis, A., Weber, T. S., van Weele, M., van der Werf, G. R., Weiss, R. F., Worthy, D., Wunch, D., Yin, Y., Yoshida, Y., Zhang, W., Zhang, Z., Zhao, Y., Zheng, B., Zhu, Q., Zhu, Q., and Zhuang, Q.: The Global Methane Budget 2000-2017, Earth Syst. Sci. Data Discuss., 2019, 1-136, 10.5194/essd-2019-128,

860 2019.

Spivakovsky, C. M., Logan, J. A., Montzka, S. A., Balkanski, Y. J., Foreman-Fowler, M., Jones, D. B. A., Horowitz, L. W., Fusco, A. C., Brenninkmeijer, C. A. M., Prather, M. J., Wofsy, S. C., and McElroy, M. B.: Three-dimensional climatological distribution of tropospheric OH: Update and evaluation, Journal of Geophysical Research: Atmospheres, 105, 8931-8980, 10.1029/1999jd901006, 2000.

865 Szopa, S., Balkanski, Y., Schulz, M., Bekki, S., Cugnet, D., Fortems-Cheiney, A., Turquety, S., Cozic, A.,

Déandreis, C., Hauglustaine, D., Idelkadi, A., Lathière, J., Lefevre, F., Marchand, M., Vuolo, R., Yan, N., and Dufresne, J.-L.: Aerosol and ozone changes as forcing for climate evolution between 1850 and 2100, Climate Dynamics, 40, 2223-2250, 10.1007/s00382-012-1408-y, 2013.

Terrenoire, E., D. A. Hauglustaine, R. Valorso, and A. Cozic, Impact of present and future aircraft NOx and aerosol emissions on atmospheric composition and radiative forcing of climate, Atmos. Chem. Phys. in preparation, 2019.

Tohjima, Y., Kubo, M., Minejima, C., Mukai, H., Tanimoto, H., Ganshin, A., Maksyutov, S., Katsumata, K., Machida, T., and Kita, K.: Temporal changes in the emissions of CH4 and CO from China estimated from CH4/CO2 and CO / CO2 correlations observed at Hateruma Island, Atmos. Chem. Phys., 14, 1663-1677, 10.5194/acp-14-1663-2014, 2014.

Turner, A. J., Frankenberg, C., Wennberg, P. O., and Jacob, D. J.: Ambiguity in the causes for decadal trends in atmospheric methane and hydroxyl, Proc Natl Acad Sci U S A, 114, 5367-5372, 10.1073/pnas.1616020114, 2017.

Turner, A. J., Frankenberg, C., and Kort, E. A.: Interpreting contemporary trends in atmospheric methane, Proceedings of the National Academy of Sciences, 116, 2805-2813, 10.1073/pnas.1814297116, 2019.

Voulgarakis, A., Naik, V., Lamarque, J. F., Shindell, D. T., Young, P. J., Prather, M. J., Wild, O., Field, R. D., Bergmann, D., Cameron-Smith, P., Cionni, I., Collins, W. J., Dalsøren, S. B., Doherty, R. M., Eyring, V., Faluvegi, G., Folberth, G. A., Horowitz, L. W., Josse, B., MacKenzie, I. A., Nagashima, T., Plummer, D. A., Righi, M., Rumbold, S. T., Stevenson, D. S., Strode, S. A., Sudo, K., Szopa, S., and Zeng, G.: Analysis of present day and future OH and methane lifetime in the ACCMIP simulations, Atmospheric Chemistry and Physics, 13, 2563-2587, 10.5194/acp-13-2563-2013, 2013.

Wolfe, G. M., Nicely, J. M., St. Clair, J. M., Hanisco, T. F., Liao, J., Oman, L. D., Brune, W. B., Miller, D., Thames, A., Gonzàlez Abad, G., Ryerson, T. B., Thompson, C. R., Peischl, J., McKain, K., Sweeney, C., Wennberg, P. O., Kim, M., Crounse, J. D., Hall, S. R., Ullmann, K., Diskin, G., Bui, P., Chang, C., and Dean-Day, J.: Mapping hydroxyl variability throughout the global remote troposphere via synthesis of airborne and satellite formaldehyde observations, Proceedings of the National Academy of Sciences, 116, 11171-11180, 10.1073/pnas.1821661116, 2019.

Zhang, Y., Jacob, D. J., Maasakkers, J. D., Sulprizio, M. P., Sheng, J. X., Gautam, R., and Worden, J.: Monitoring global tropospheric OH concentrations using satellite observations of atmospheric methane, Atmos. Chem. Phys., 18, 15959-15973, 10.5194/acp-18-15959-2018, 2018.

Zhao, Y., Saunois, M., Bousquet, P., Lin, X., Hegglin, M. I., Canadell, J. G., Jackson, R. B., Hauglustaine, D. A., Szopa, S., Stavert, A. R., Abraham, N. L., Archibald, A. T., Bekki, S., Deushi, M., Jöckel, P., Josse, B., Kinnison, D., Kirner, O., Maréčal, V., O'Connor, F. M., Plummer, D. A., Revell, L. E., Rozanov, E., Stenke, A., Strode, S., Tilmes, S., Dlugokencky, E. J., and Zheng, B.: Inter-model comparison of global hydroxyl radical (OH) distributions and their impact on atmospheric methane over the 2000-2016 period, Atmos. Chem. Phys. Discuss., 2019, 1-47, 10.5194/acp-2019-281, 2019.

Zheng, B., Chevallier, F., Yin, Y., Ciais, P., Fortems-Cheiney, A., Deeter, M. N., Parker, R. J., Wang, Y.,

Worden, H. M., and Zhao, Y.: Global atmospheric carbon monoxide budget 2000–2017 inferred from multi-species atmospheric inversions, Earth Syst. Sci. Data, 11, 1411-1436, 10.5194/essd-11-1411-2019, 2019.

905

Tables

Table 1. Global tropospheric mean [OH] and inter-hemispheric OH ratios (N/S) averaged over 2000-2002 for 10 OH fields used in this study. The global tropospheric [OH] weighted by reaction with CH_4 ($[OH]_{GM-CH4}$) and weighted by dry air-mass ($[OH]_{GM-M}$) are both given.

	$[OH]_{GM-CH4}$	$[OH]_{GM-M}$	N/S
TransCom	10.6	10.0	1.0
INCA NMHC-AER-S	10.3	9.4	1.3
INCA NMHC	11.1	10.4	1.2
CESM1-WACCM	11.9	11.4	1.3
CMAM	12.2	11.3	1.2
EMAC-L90MA	11.8	11.5	1.2
GEOSCCM	12.6	12.3	1.2
MOCAGE	15.0	12.5	1.5
MRI-ESM1r1	10.9	10.6	1.2
SOCOL3	16.3	14.4	1.5
Mean±SD	12.3±3.8	11.4±2.8	1.3±0.3
Mean±SD (8 OH)[1]	11.3±0.8	10.9±0.9	1.2±0.1

[1] The OH fields simulated by SOCOL3 and MOCAGE are excluded.

Table 2. The global total and hemispheric CH_4 emissions calculated with the 10 original OH fields (Inv1), and inter-hemispheric difference of CH_4 emissions calculated by Inv1 and Inv2 (scaled OH fields) during the early 2000s (2000/07/01-2002/06/01).

	Global	**0-90 N**	**90 S-0**	**N-S_Inv1**	**N-S_Inv2**
Prior	522	384	138	246	246
TransCom	530	368	162	206	205
INCA NMHC-AER-S	518	380	138	242	245
INCA NMHC	552	392	160	232	232
CESM1-WACCM	587	420	166	254	249
CMAM	599	419	180	239	245
EMAC-L90MA	589	414	175	239	237

GEOSCCM	611	424	187	237	233
MOCAGE	716	/[a]	/	/	/
MRI-ESM1r1	553	396	156	240	244
SOCOL3	757	/	/	/	/
Mean±SD	601±78	401±21	166±15	236±14	236±14

[a] We do not analyze the hemispheric CH_4 emission estimated with MOCAGE and SOCOL3 OH field since inversions using the two OH fields calculate much higher CH_4 emissions than using other OH fields.

Table 3. Regional CH_4 emissions (mean±SD) calculated by Inv1 and Inv2, and for the prior emissions during the early 2000s (2000/07/01-2002/06/01) in Tg yr^{-1}.

Region	Inv1	Inv2	Prior
North America(USA)	45±2	45±1	42
Canada(CAN)	27±1	27±1	33
Europe(EU)	27±1	27±1	29
Russia(RUS)	33±1	33±1	31
China(CHN)	42±5	40±3	51
Southeast Asia(SEAS)	38±3	37±0.3	33
South Asia(SAS)	59±6	57±0.8	44
Northern South America(NSA)	73±9	69±4	56
Southern South America(SSA)	33±4	31±2	27
Africa(AF)	76±4	74±1	65

Table 4. Global and latitudinal percentage changes of CH_4 reaction weighted [OH] from 2000-2002 to 2007-2009.

	90-30 °S	30 °S-0 °	0 °-30 °N	30 °-90 °N	Global
TransCom	0.0%	0.0%	0.0%	0.0%	0.0%
INCA NMHC	-0.5%	-0.9%	-0.3%	-0.2%	-0.5%
CESM1-WACCM	1.1%	1.6%	2.5%	1.2%	1.8%
EMAC-L90MA	-0.1%	0.1%	1.3%	1.1%	0.7%
GEOSCCM	-0.3%	1.1%	1.4%	1.0%	1.0%
MRI-ESM1r1	-2.0%	0.2%	2.4%	1.7%	1.1%

Table 5. Global total emission changes (in Tg yr^{-1}) from the early 2000s (2000/07/01-2002/06/01) to the
late 2000s (2007/07/01-2009/06/01) calculated to identify the effect of OH fields (E_change_all, Inv3－
Inv2), of OH fixed to early 2000s (E_change_fixoh, Inv4－Inv2), and the contribution of OH changes
from the early to late 2000s to top-down estimated CH$_4$ emissions changes (E_change_varoh, Inv4－
Inv3).

	Inv3－Inv2 E_change_all	Inv4－Inv2 E_change_fixoh	Inv3－Inv4 E_change_varoh
TransCom	17.2	17.2	0.0
INCA NMHC	16.6	19.3	-2.7
CESM1-WACCM	30.0	18.5	11.5
EMAC-L90MA	20.4	15.3	5.1
GEOSCCM	19.1	16.1	3.0
MRI-ESM1r1	27.8	14.3	13.5
Mean±SD	21.9±5.7	16.9±1.9	5.1±6.4

Table 6. Global sectoral emission changes (in Tg yr^{-1}) from the early 2000s (2000/07/01-2002/06/01) to
the late 2000s (2007/07/01-2009/06/01) (mean±SD).

	Inv3－Inv2 E_change_all	Inv4－Inv2 E_change_fixoh	Inv3－Inv4 E_change_varoh	Prior
Wetland	-3.5±2.5	-5.6±1.3	2.1±3.4	0.0
Agri-waste	14.2±2.1	12.3±0.7	1.9±2.3	19.0
Fossil fuel	8.7±0.8	8.1±0.8	0.6±0.9	18.0
Other	2.4±0.5	2.0±0.2	0.5±0.5	2.5
Total	21.9±5.7	16.8±1.9	5.1±6.4	39.4

945 **Figures**
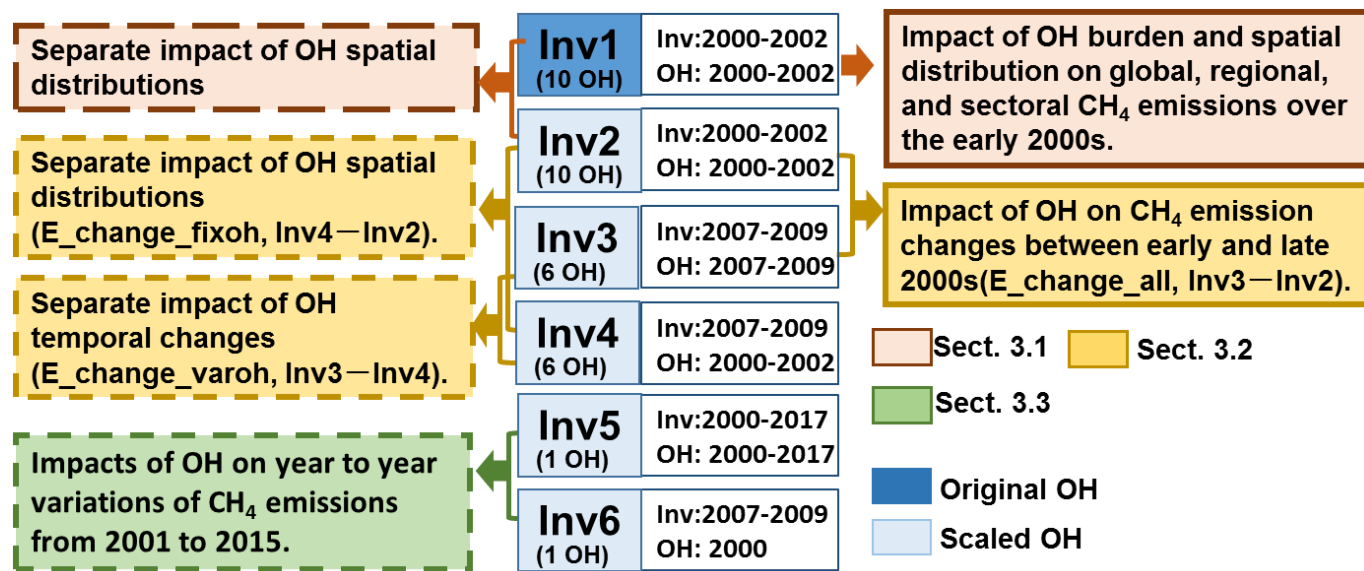
Figure 1. A diagram showing inversion experiments (Inv1–Inv6) performed in this study. For each experiment, "Inv" gives the time period of inversion, and "OH" gives the time period of the OH fields
950 used in the inversion. Inv1 is performed using the original OH field, whereas Inv2-Inv5 are performed using scaled OH fields. The colored boxes on the left and right show analyses of inversions we did to examine the OH impacts on inverted CH_4 emissions. The brown, yellow, and green textboxes correspond to analyses presented in Section 3.1, Section 3.2, and Section 3.3, respectively.

955

Atmospheric
Chemistry
and Physics
Discussions
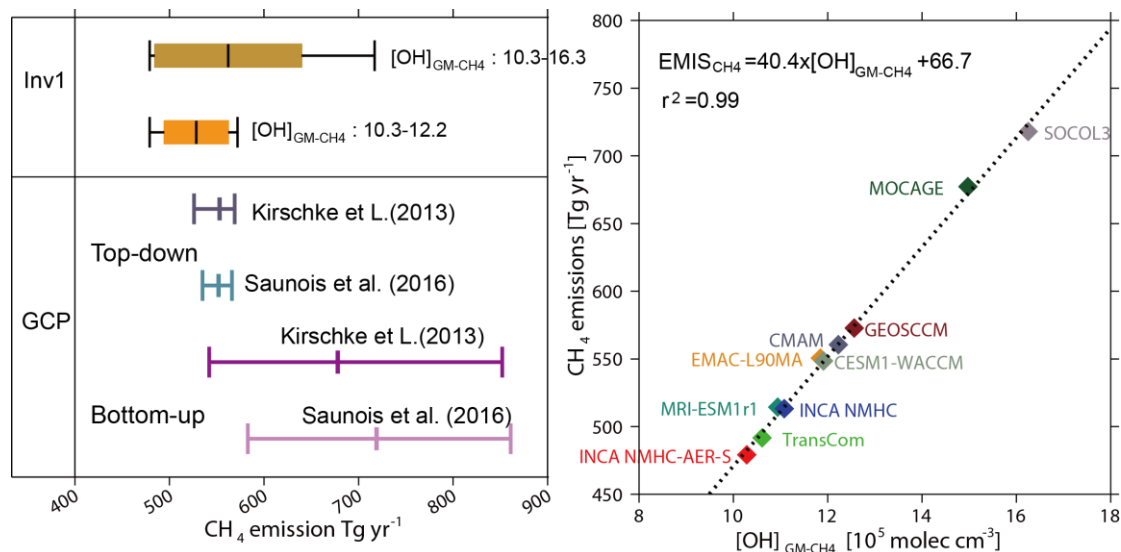
Figure 2. Left: The global CH₄ emissions from Inv1 (averaged over 2000/07/01-2002/06/01). The bottom-up and top-down estimations over 2000-2009 from previous GCP (Kirschke et al., 2013; Saunois et al., 2016) are also presented for comparison. The brown box plot shows the inversion results using 10 OH fields, while the orange one shows the results that exclude the largest estimates from the SOCOL3 and MOCAGE OH fields. The left, middle and right whisker chart (vertical lines) represent the minimum, mean, and maximum values of different inversion, and the left and right edges of boxes represent the mean ±one standard deviation. The definition of the box plot is applicable to all those hereafter. Right: The relationship between the optimized CH₄ emissions (Tg yr^{-1}) in Inv1 and the corresponding $[OH]_{GM-CH4}$ ($\times 10^5$ mole cm^{-3}) . The correlation coefficient (r) and the linear regression equation fitted to the data are shown inset.
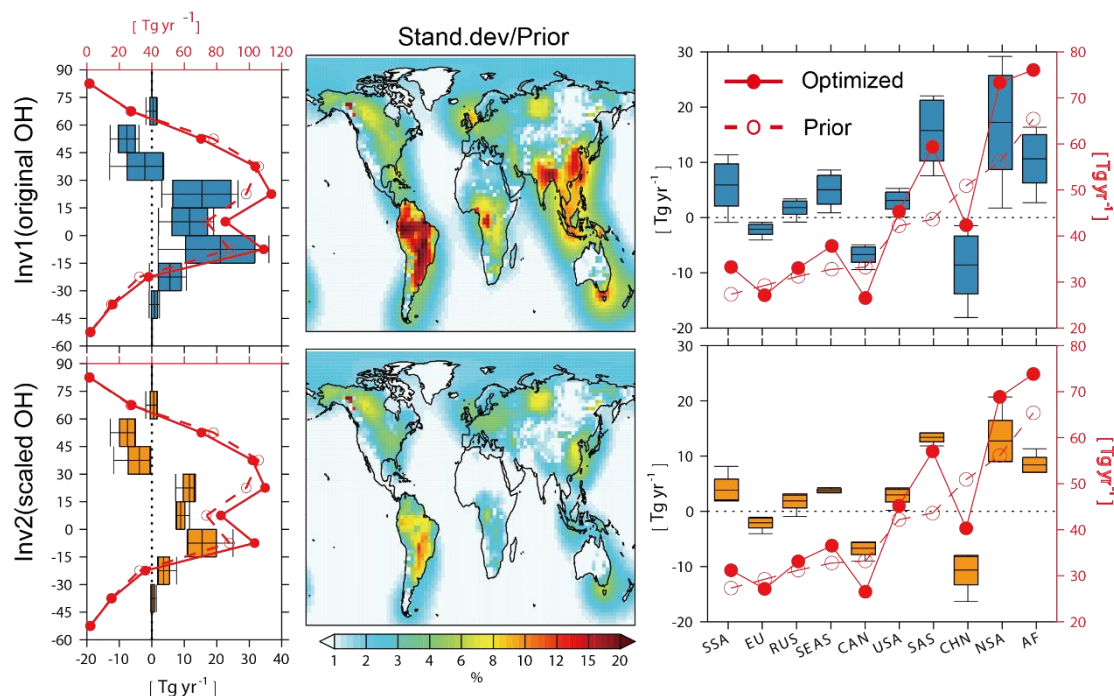
Figure 3. Zonal (left), and regional averages (right) of CH$_4$ emissions calculated by Inv1 (top row) and Inv2 (bottom row) with 8 OH fields from 2000/07/01 to 2002/06/01. Left and right panels: prior (dash red line) and mean optimized (solid red line) CH$_4$ emissions for every 15-degree latitudinal band and 10 regions, respectively. Where USA=North America, CAN=Canada, EU=Europe, RUS=Russia, CHN=China, SEAS=Southeast Asia, SAS=South Asia, NSA=northern South America, SSA=southern South America, AF=Africa. The full names of the abbreviations are applicable to all figures hereafter. The differences between prior and optimized emissions (optimized minus prior) are shown by the box plots (defined in Fig. 1). Prior and optimized emissions values correspond to the right axes and their differences correspond to the left axes. Middle panel: the ratio of the standard deviation of emissions in each grid-cell calculated by Inv1 (top) and Inv2 (bottom) to prior emissions.
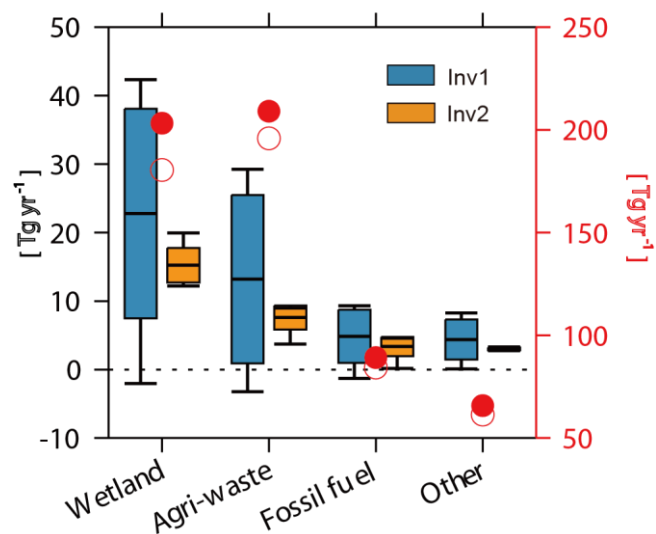
Figure 4. Global total CH$_4$ emissions from four broad categories from 2000/07/01-2002/06/01 in Tg yr^{-1}. The red circles and dots show the prior emissions and mean optimized emissions, respectively, as calculated by Inv1 (right axes), and the box plots (defined in Fig. 1) show the difference between optimized emissions calculated by Inv1 (blue) and Inv2 (yellow) and prior emissions (optimized minus prior, left axes).
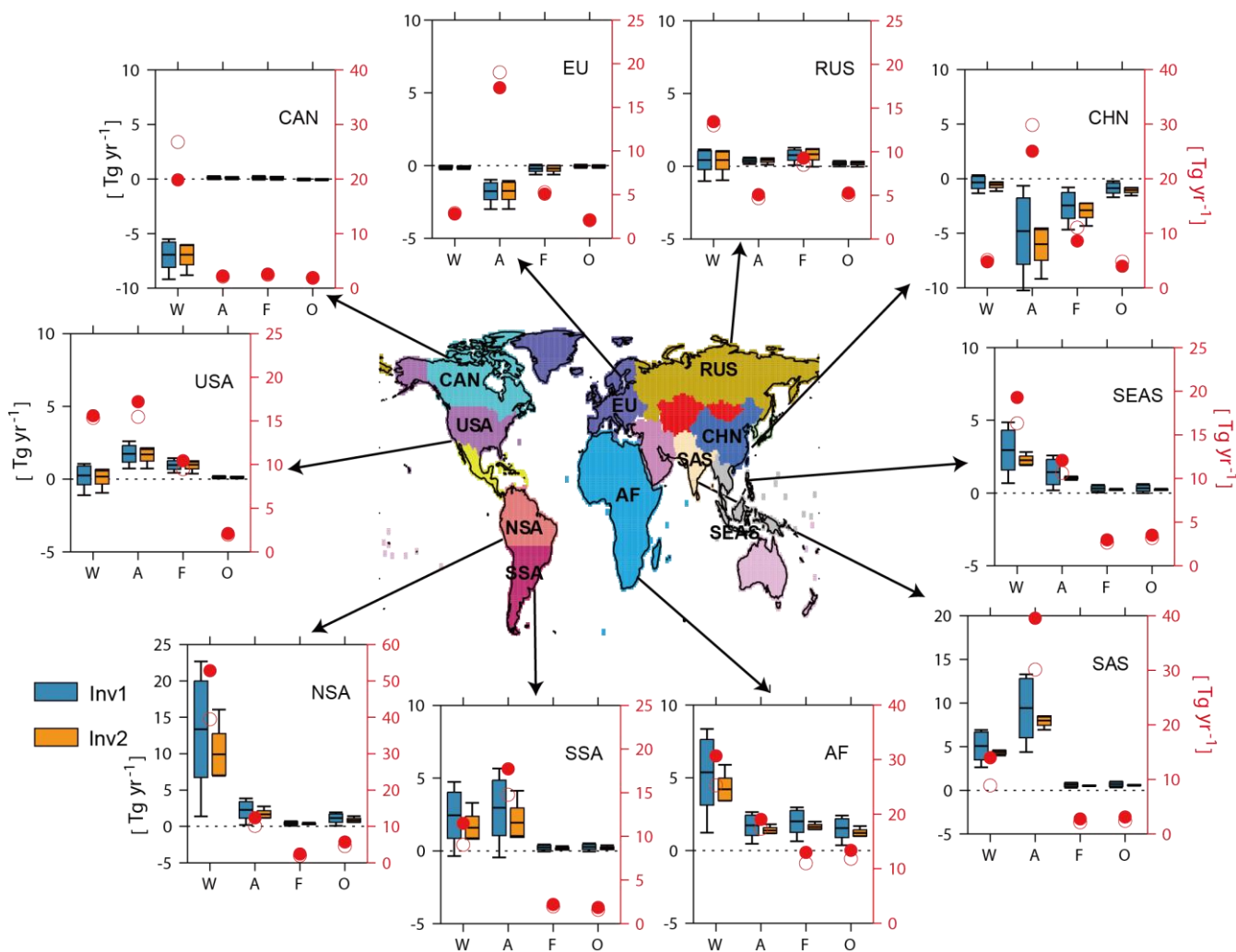
Figure 5. Same as Fig. 4 but for prior and optimized emissions over 10 emitting regions covering most of the emitting lands. W=Wetlands, A=Agri-waste, F=Fossil fuels, and O=Others. In Tg yr^{-1}.

995
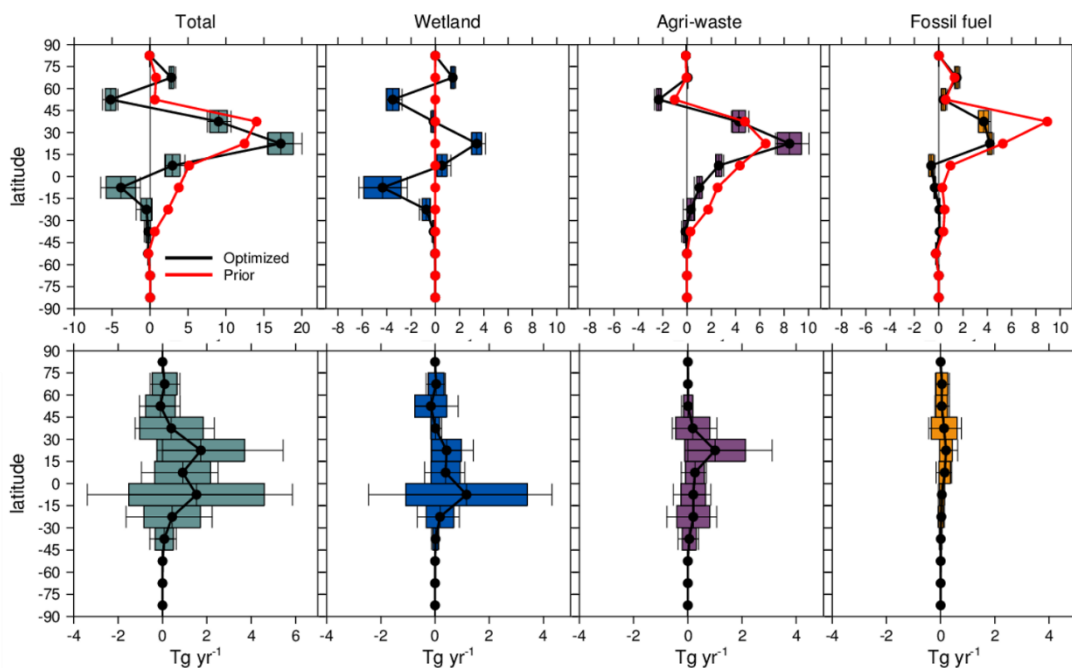
Figure 6. Top panel: latitudinal emission (every 15-degree latitudinal band) changes in Tg yr^{-1} from the early 2000s (2000/07/01-2002/06/01) to the late 2000s (2007/07/01-2009/06/01) of total, wetlands, agriculture and waste, and fossil fuel emissions (E_change_all, Inv3－Inv2). Bottom panel: contribution of OH changes on top-down estimated CH$_4$ emission changes between the two periods (E_change_varoh, Inv3－Inv4). The red lines are changes of prior emissions and the black lines are the mean changes of optimized emissions. The box plots (defined by Fig. 1) show the uncertainties and ranges calculated with different OH fields.

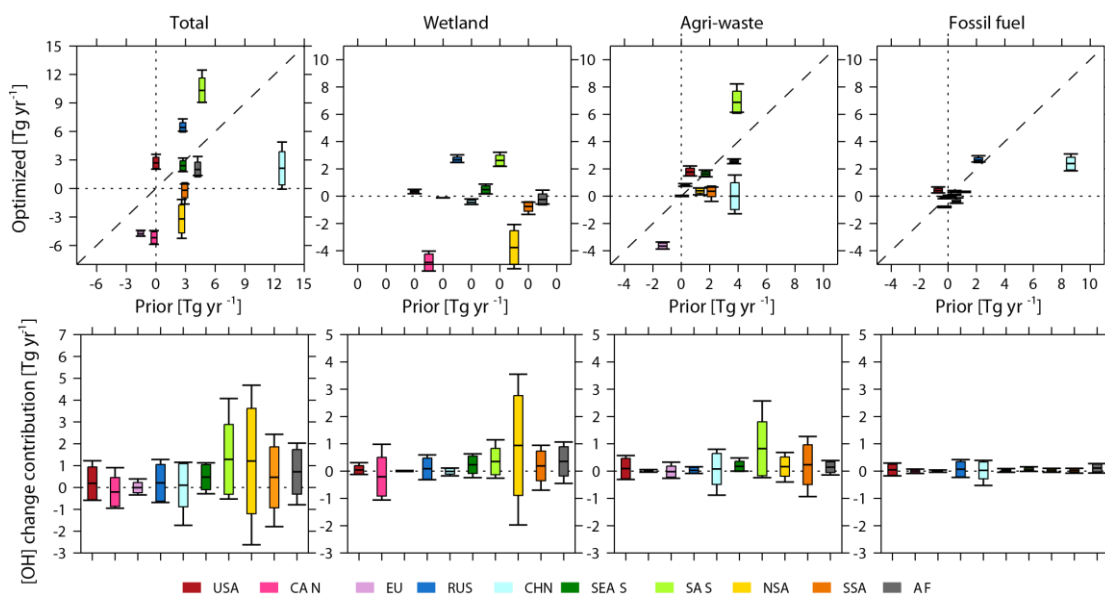**Figure 7.** Top panel: optimized global total and sectoral regional emission changes in Tg yr^{-1} from the early 2000s to the late 2000s (y-axis) plotted against prior emission changes between the two time periods (x-axis) as derived from Inv3 and Inv4(E_change_all). The prior wetland emissions are constant over time, thus show zero changes (all '0' on the x-axis). Bottom panel: contribution of OH changes between the two periods on top-down estimated emission changes (E_change_varoh). The box plots (defined by Fig. 1) show the uncertainties and ranges calculated with different OH fields.
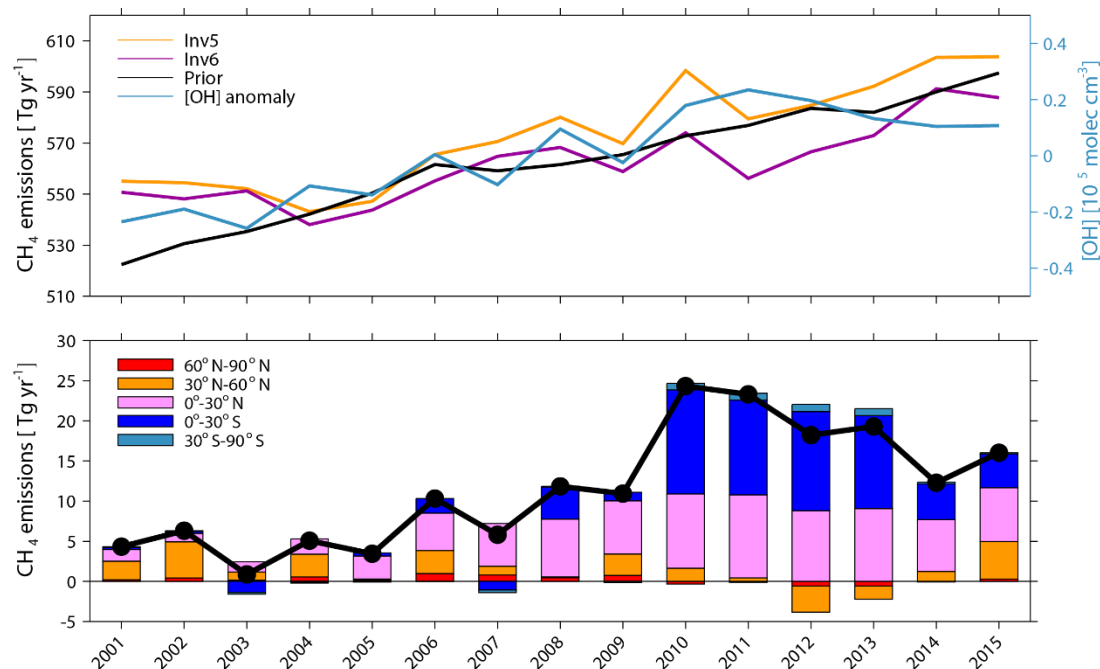
Figure 8. Top panel: Time series of global total CH_4 emissions calculated by Inv5 (yellow) and Inv6 (purple) plotted together with prior emissions (black), and $[OH]_{GM-CH4}$ anomaly of CESM OH fields (blue). Bottom panel: the difference of global total (black line) and latitudinal (stack bar plots) CH_4 emissions between Inv5 and Inv6 (Inv5-Inv6).
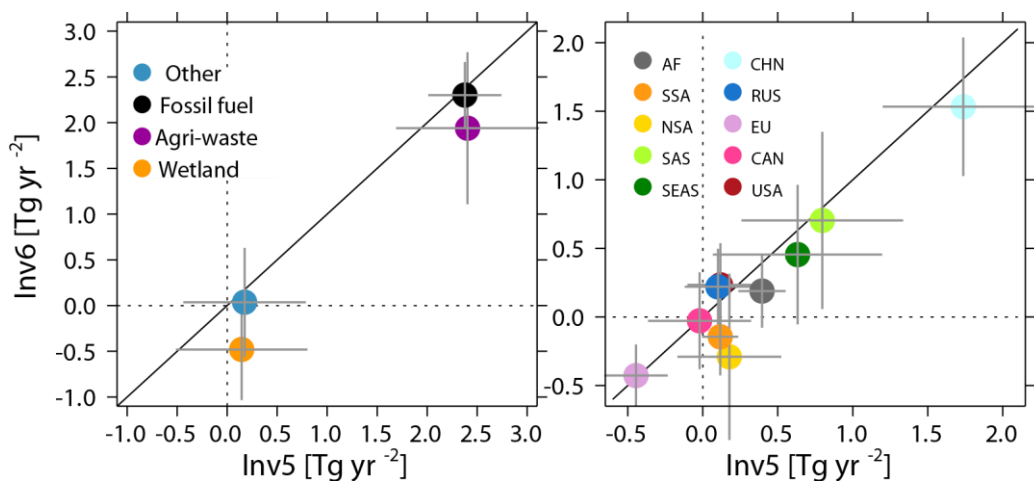

Figure 9. Comparison between Inv5 (x-axis) and Inv6 (y-axis) estimated global total CH_4 emissions trends in Tg yr^{-2} between 2004 and 2015 for the four categories (left) and over the ten continental regions (right). The error bars show the trend with 95% confidence intervals.